OPTIMIZATION OF STRETCHABLE FINGERNAIL SENSOR DESIGN FOR FINGERTIP FORCE DIRECTION ESTIMATION

by

Jumana M. Abu-Khalaf

A dissertation submitted to the faculty of
The University of Utah
in partial fulfillment of the requirements for the degree of

Doctor of Philosophy

Department of Mechanical Engineering

The University of Utah

May 2012

Copyright © Jumana M. Abu-Khalaf 2012

All Rights Reserved

The University of Utah Graduate School

STATEMENT OF DISSERTATION APPROVAL

The dissertation of **Jumana M. Abu-Khalaf**

has been approved by the following supervisory committee members:

Stephen Mascaro	, Chair	**3/13/2012** Date Approved
Stacy Bamberg	, Member	**3/09/2012** Date Approved
John Hollerbach	, Member	**3/19/2013** Date Approved
Sanford Meek	, Member	**3/13/2012** Date Approved
Debra Mascaro	, Member	**3/13/2012** Date Approved

and by **Timothy Ameel**, Chair of the Department of **Mechanical Engineering**

and by Charles A. Wight, Dean of The Graduate School.

ABSTRACT

The optimization of novel stretchable fingernail sensors for detecting fingertip touch force direction is introduced. The fingernail sensor uses optical reflectance photoplethysmography to measure the change in blood perfusion in the fingernail bed when the finger pad touches a surface with various forces. This "fingernail sensing" technique involves mounting an array of LEDs (Light Emitting Diodes) and photodetectors on the fingernail surface to detect changes in the reflection intensity as a function of applied force. The intensity changes correspond to changes in blood volume underneath the fingernail and allow for fingertip force detection without haptic obstruction, which has several applications in the area of human-machine interaction.

This dissertation experimentally determines the optimal optical parameters for the transmittance of light through the human fingernail bed. Specifically, the effect of varying the wavelength and optical path length on light transmittance through the nail bed are thoroughly investigated. Light transmittance through the human fingernail is optimized when using green light (525nm) and when placing optoelectronic pairs as close together as possible. The optimal locations of the optoelectronic devices are predicted by introducing an optical model that describes light transmittance between an LED and a photodiode in the fingernail area based on optical experimentation. A reduced configuration is derived from the optimal optoelectronic locations in order to facilitate

the fabrication of the optimized fingernail sensor without significantly compromising the recognition accuracy. This results in an overall force direction recognition accuracy of 95%. Using novel fabrication techniques, we successfully build a stretchable fingernail sensor prototype, which fully conforms to the two-dimensional fingernail surface and is independent of its geometry. Namely, we overcome the challenges of patterning conductive lines on a stretchable substrate, and embedding rigid optical components in a stretchable platform while maintaining electrical conductivity. A finite element analysis is conducted to optimize the electrical contact resistance between the optoelectronic components and underlying stretchable conductors, as a function of the bending curvature and substrate thickness. The functionality of the stretchable sensor is tested in relation to the design parameters. Finally, applications and potential impacts of this work are discussed.

TABLE OF CONTENTS

LIST OF TABLES

ACKNOWLEDGMENTS

I would like to thank my very supportive family for their incredible love and encouragement. I am forever grateful to my dad from whom I inherit the thirst for learning, to my mom who inspired me to pursue my academic journey, and to my siblings and friends who have been the best support system for these last few years. My loving fiancé Sameer, there aren't enough words to express my love and appreciation for your support, encouragement, and patience. All I can say is thank you for making this last year the best that I have had.

I wish to thank my advisor, Stephen Mascaro, for his guidance and support throughout my research experience, as well as my graduate committee members for their valuable input. I would also like to thank all members of the BioRobotics and BioInstrumentation labs for their help, suggestions, and many inspiring discussions. Special thanks go to Debra Mascaro, Stacy Bamberg, and Minu Gandhi for their much appreciated support and friendship.

Above all, I thank my Creator The most knowledgeable, The most expert, and The most wise for blessing me with faith and patience in my quest of knowledge.

CHAPTER 1

INTRODUCTION

Measurement of fingertip touch forces plays a key role in the fields of haptics, robotics and virtual reality [1]. In particular, it has several applications in the area of human-machine interaction, such as operating a machine using virtual switches based on simple on/off detection of touch force [2]. It is also useful for robot teleoperation and acquiring human skills to train robots to perform complex assembly tasks [3, 4]. In addition, it contributes to the study of human grasping and manipulation as well as characterizing the human haptic sense [5, 6].

Typically, normal and shear forces acting on the fingertips have been measured using electronic gloves with force-sensing pads [7]. However, this method was found to have an undesirable effect on the human haptic sense as it forms a barrier between the human fingers and the surrounding environment. In previous work, Mascaro and Asada proposed a new sensing approach which allows for full range of haptic sense by mounting optical reflectance photo-plethysmograph sensors on the fingernail [8]. In their work, they also established that distinct patterns of color changes occur along the fingernail area as the fingertip is pressed down against a planar surface [9]. The pattern of observable color changes is directly related to changes in the blood volume in the nail

bed, which varies as a function of applied force, and allows for fingertip force detection without haptic obstruction.

Research Background

Measurement Principle

Fingernail sensors have been developed for detecting fingertip touch force and finger posture based on the reflectance photoplythysmography technique [8], illustrated in Figure 1.1(a). An array of LEDs and photodetectors, implemented in the sensor, was used to measure variations in capillary blood volume as a function of applied force. In principle, LEDs illuminate the fingernail area while nearby photodetectors detect the reflected light intensity resulting in output voltages, which vary with applied force, from the photodetector's circuit, shown in Figure 1.1(b).

Fingernail Coloration Patterns

Distinct patterns of color changes occur along the fingernail area as the fingertip is pressed down against a planar surface [9]. The pattern of observable color changes is

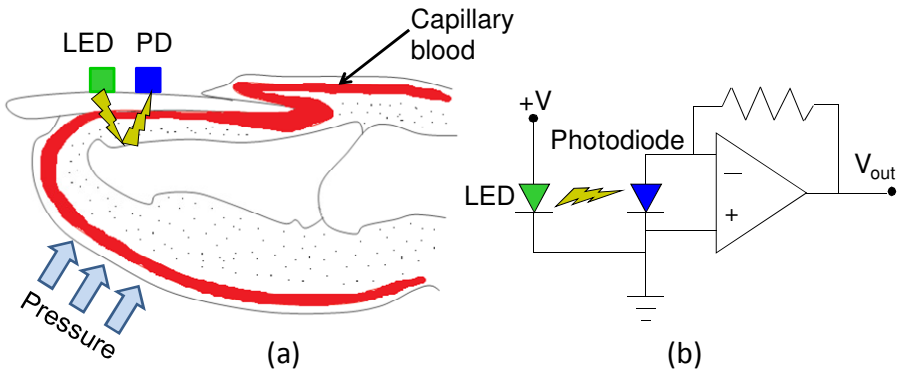

Figure 1.1 Fingernail sensor principle of operation. (a) LED and photodiode used to measure variations in fingernail coloration using (b) plethysmograph circuitry.

directly related to changes in the blood volume in the nail bed, which varies as a function of applied force. In fact, fingernail coloration patterns were found to be significantly distinct for 6 different types of fingertip force [9].

The photographic catalog shown in Figure 1.2 represents average fingernail coloration patterns of 15 human subjects. The first image is the nominal pose where no force is applied on the fingertip. In the second image, a normal force of -3N is applied. Next, lateral and longitudinal shear forces of 2N, applied in the positive and negative directions, are added. The resulting average fingernail coloration patterns were found to be generally representative of the population [9].

Original Fingernail Sensor Design

In the original fingernail sensor, color changes observed through the fingernail have been measured by mounting an array of 6 LEDs and 8 photodetectors on the

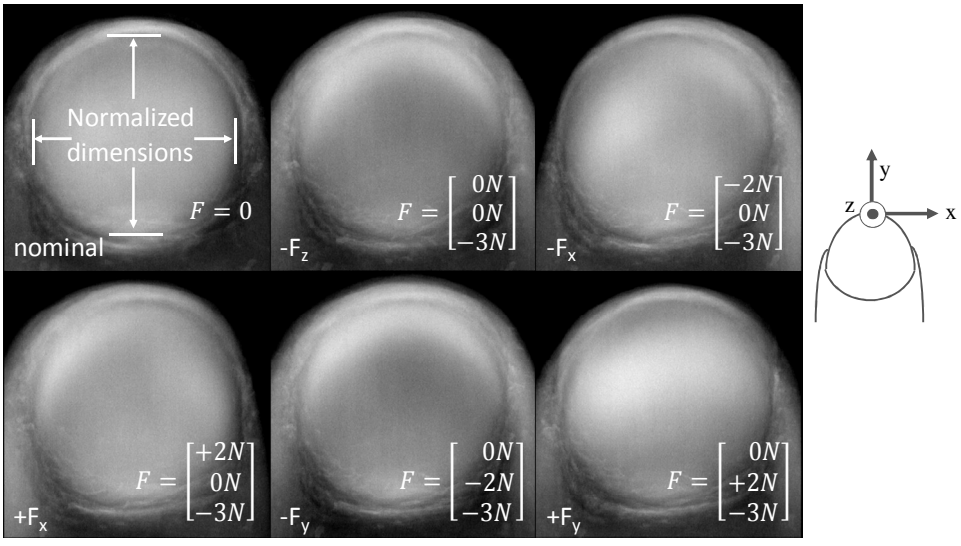

Figure 1.2 Average fingernail coloration patterns for 15 human subjects for 6 different force poses. Images were collected by S. Mascaro and H. Asada [9]. 5x contrast is applied for visual illustration.

fingernail in a laterally symmetric configuration, as shown in Figure 1.3(a). To ensure that each photodiode has at least one neighboring LED, the LEDs were placed between the photodiodes. The role of each of the photodetectors was investigated in terms of the effect of removing one or more on force estimation. The analysis suggested designing the next generation of fingernail sensors with fewer photodetectors, as shown in Figure 1.3(b).

The original fingernail sensor had the capability of measuring normal and shear touch forces, as well as finger posture, while removing or reducing undesired effects of other extraneous variables. The miniaturized sensor was tested and analyzed by using experimental apparatus, which measures actual 3-axis fingertip touch forces and finger posture. The response of the prototype sensor was characterized for different types of forces, where the sensor responded with different patterns to each of the variables of interest [10].

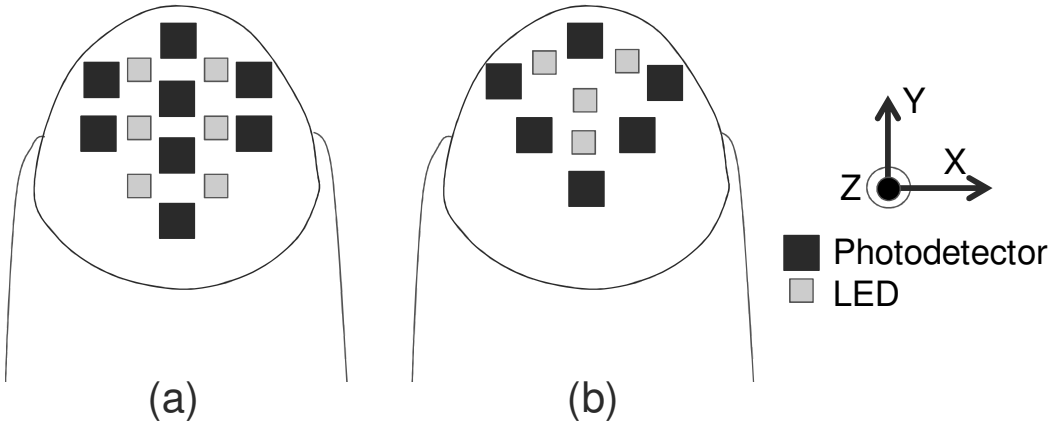

Figure 1.3 Spatial optoelectronic configuration. (a) Original fingernail sensor and (b) recommended configuration for next generation of fingernail sensors.

In the original design, miniaturized die-form optical and electrical components were mounted on a flexible Kapton printed circuit board (PCB), using wire bonding. LEDs having a peak emission wavelength of 770nm were used to remove the dependence of the light absorption coefficient of blood on oxygen saturation. To eliminate direct illumination between the emitters and detectors, optically opaque epoxy was placed between them. To mold the sensor to the shape of the user's fingernail, a layer of optically transparent epoxy, which covered the LEDs and photodiodes, was used. Amplifiers were placed on the top surface of the sensor, which was completely coated with optically opaque epoxy to shield the optoelectronics from ambient light. Figure 1.4 demonstrates a fully functional fingernail sensor assembled in rigid PCB.

The sensor was tested for several human–machine interface applications demonstrating potential impact on the fields of robotics and virtual reality. Calibration experiments were performed to train and validate a linear predictor for 7 human subjects, based on readings from the fingernail sensor array of 6 LEDs and 8 photodetectors [10].

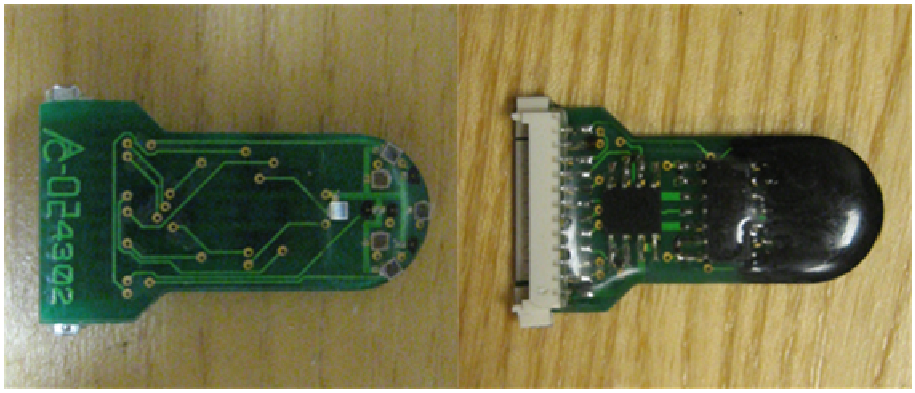

Figure 1.4 Implementation of original fingernail sensor. In the left picture, the optoelectronic devices are mounted on the bottom side of the sensor. In the right picture, the amplifiers are placed on the top side.

Random testing results showed that on average, shear forces and normal forces can be predicted with a root mean square error (rms) of 0.5N and 1N, respectively. The average rms error in the measurement of shear forces is approximately 10% of the shear force range, making it useful for human-machine interaction. However, the large average rms error of the normal force is unsatisfactory and limits the utility of the sensors, as the range of normal forces is only 0-3N. Therefore, to allow the sensor to be more useful, a more intelligent configuration of the LEDs and photodetectors is required as it is anticipated to improve the sensor's performance for the variables of interest.

Imaging the Fingernail and Surrounding Skin

An alternative approach for measuring fingertip touch forces, proposed by Sun, Hollerbach and Mascaro [11], uses an external camera system to image the fingernail and surrounding skin. Results indicated a complex pattern of coloration under applied force across the fingernail area and surrounding skin. Particularly, the middle region of the fingernail has a low force range (0-2N), the front region has an intermediate force range (2-6N), while the skin has a high force range (3-6N). By imaging the coloration changes in the fingernail and skin, normal and shear fingertip touch forces can be estimated with an accuracy of 5%-10% for a force range up to 10N. Further experiments have been conducted to infer fingertip force direction during planar contact [12, 13], where fingernail images of 15 human subjects were registered to reference images and then warped to an atlas to extract common coloration features corresponding to force direction. This resulted in an overall force direction recognition accuracy of 94%.

In comparison to the results obtained using the original fingernail sensor, the fingernail imaging approach produced more accurate results and double the range of forces that can be measured. On the other hand, the use of an external camera system presents challenges of keeping the fingernail in view, and handling image registration, none of which is an issue with the original sensor.

Proposal and Overview

In this dissertation, the optimization of novel stretchable fingernail sensors for detecting fingertip touch force direction is introduced. The proposed research builds on previous work by Mascaro and Asada, where a novel force sensing approach using optical reflectance photoplethysmograph sensors mounted on the fingernail, was introduced. This sensing technique involves mounting an array of LEDs and photodetectors on the fingernail surface to detect changes in the changes in blood volume underneath the fingernail which vary as a function of applied force.

Specifically, the optimal optical parameters for the transmittance of light through the human fingernail bed are experimentally determined in order to optimize detection of blood volume variations in the nail bed. Based on optical experimentation, an optical model, which describes light transmittance between an LED and a photodiode in the fingernail area, is used to predict the optimal locations of the optoelectronic devices. The resulting optimal optoelectronic configuration is validated and anticipated to improve the sensor's force direction estimation capabilities. The original fingernail sensor was rigidly attached to the human fingernail, necessitating a customized fabrication for each

individual user. To overcome this disadvantage, a stretchable senor prototype, which is independent of the fingernail geometry, is developed using novel fabrication techniques.

First, in Chapter 2, light transmittance through the fingernail is thoroughly investigated in relation to varying the LED wavelength and optical path length between an optoelectronic pair. Detailed experimental characterization of the sensitivity and efficiency of light transmittance through the fingernail bed to wavelength and optical path length is performed. This results in determining the optical parameters for the transmittance of light through the human fingernail bed, which optimize detection of blood volume variations in the nail bed. In Chapter 3, an optimal redesign of the optoelectronic configuration of the fingernail sensor is proposed in order to optimize force direction distinguishability between the variables of interest. This is achieved by introducing an experimentally-calibrated optical model which describes light transmittance between an LED and a photodiode in the fingernail area. The resulting optimal optoelectronic configuration was validated by examining its ability to classify the correct force direction of test images. A reduced configuration was derived from the optimal optoelectronic locations in order to facilitate the fabrication of the optimized fingernail sensor without significantly compromising the classification accuracy. In Chapter 4, a stretchable fingernail sensor prototype is designed to fully conform to the two-dimensional curvature of the human fingernail, while maintaining electrical conductivity. Novel fabrication techniques are introduced to overcome the challenges of patterning conductive lines on a stretchable substrate, and embedding rigid optical components in a stretchable platform, while maintaining electrical conductivity. The fabrication of the stretchable fingernail sensor is optimized based on finite element

modeling, where the electrical conductivity between the optoelectronic devices and the underlying stretchable conductors is investigated. The functionality of the proposed sensor design was examined in relation to the bending curvature and the substrate thickness. Finally, in Chapter 5, the contributions of this dissertation are summarized and future work is proposed.

References

[1] J.G. Webster, Ed., Tactile Sensors for Robotics and Medicine. New York: Wiley, 1988.

[2] S. Mascaro and H. Asada, "Virtual switch human-machine interface using fingernail touch sensors," *Proc. IEEE Int. Conf. Robotics and Automation*, vol. 4, pp. 2533-2538, 1999.

[3] S. Mascaro and H. Asada, "Hand-in-glove human-machine interface and interactive control: Task process modeling using Petri Nets," *Proc. IEEE Int. Conf. Robot. Automat.*, vol. 2, pp. 1289–1295, 1998.

[4] H. Yun, D. Cannon, A. Freivalds, and G. Thomas, "An instrumented glove for grasp specification in virtual-reality-based point-and-direct telerobotics," *IEEE Trans. Syst. Man, Cybern. B*, vol. 27, pp. 835–846, 1997.

[5] S. Sato, M. Shimojo, Y. Seki, A. Takahashi, and S. Shimuzu, "Measuring system for grasping," *Proc. IEEE Int. Workshop Robot Human Commun.*, pp. 292–297, 1996.

[6] I. Kim and H. Inooka, "Determination of grasp forces for robot hands based on human capabilities," *Contr. Eng. Practice*, vol. 2, no. 3, pp. 415–420, 1994.

[7] D.J. Sturman and D. Zelzer, "A survey of glove-based input," *IEEE Computer Graphics & Applications*, pp. 30-39, January, 1994.

[8] S. Mascaro and H. Asada, "Photoplethysmograph fingernail sensors for measuring finger forces without haptic obstruction," *IEEE Trans. on Robotics and Automation*, vol. 17, no. 5, pp. 698–708, 2001.

[9] S. Mascaro and H. Asada, "The common patterns of blood perfusion in the fingernail bed subject to fingertip touch force and finger posture," *Haptics-e: The Electronic Journal of Haptics Research*, vol. 4, no. 3, pp. 1-6, 2006.

[10] S. Mascaro and H. Asada, "Measurement of finger posture and three-axis fingertip touch force using fingernail sensors," *IEEE Trans. on Robotics and Automation*, vol. 20, no. 1, pp. 26-35, 2004.

[11] Y. Sun, J. Hollerbach, and S. Mascaro, "Predicting fingertip forces by imaging coloration changes in the fingernail and surrounding skin," *IEEE Transactions on Biomedical Engineering*, vol. 55, no. 10, pp. 2363-2371, 2008.

[12] Y. Sun, J. Hollerbach, and S. Mascaro, "Imaging the finger force direction," *IEEE Computer Society Conference on Computer Vision and Pattern Recognition (CVPR)*, pp. 1-6, June 18-23, 2007.

[13] Y. Sun, J. Hollerbach, and S. Mascaro, "Estimation of finger force direction with computer vision," *IEEE Transactions on Robotics*, vol. 25, no. 6, pp. 1356-1369, 2009.

CHAPTER 2

OPTIMIZATION OF FINGERNAIL SENSOR DESIGN BASED ON OPTICAL EXPERIMENTATION

Abstract

The purpose of this paper is to experimentally determine the optimal optical parameters for the transmittance of light through the human fingernail bed in order to measure the change in blood volume beneath the fingernail when force is exerted on the fingertip. This "fingernail sensing" technique is a form of photo-plethysmography and it involves the placement of LEDs and photodetectors on the fingernail surface. When forces are applied to the fingertip, the blood perfusion in the fingernail bed is affected resulting in various red and white coloration regions observed through the fingernail. Thus, the transmittance of light through the fingernail bed is a function of applied force, which results in a change in voltage from the photodetector circuit. Previously, much research has been done to build and calibrate black-box models that estimate fingertip touch force based on the photodetector outputs. However, the effect of varying the wavelength and optical path length on light transmittance through the nail bed has not been thoroughly investigated. Due to recent advances in the manufacturing of fingernail sensors and the availability of surface mount LEDs of certain wavelengths, we now perform a thorough experimental characterization of the sensitivity and efficiency of light

transmittance through the fingernail bed to wavelength and optical path length. Results show that the optical parameters for the transmittance of light through the human fingernail bed are optimized when using green light (525nm) and when the surface mount LED and photodiode are placed as close together as possible.

Introduction and Background

A novel sensing approach for fingertip touch force detection was introduced by Mascaro and Asada in [1], where patterns of blood perfusion in the fingernail bed were measured using optical reflectance photo-plethysmograph sensors mounted on the fingernail. When the finger pad touches a surface with various forces, distinct patterns of color changes occur along the fingernail as a result of blood volume variations in the nail bed [2]. An array of LEDs and photodetectors, implemented in the sensor, was used to measure and distinguish between the variables of interest. In principle, LEDs illuminate the fingernail area while nearby photodetectors detect the reflected light intensity resulting in output voltages, which vary with applied force, from the photodetectors circuit [1].

Fingernail sensors can be used in several applications in the area of human-machine interaction, such as using these sensors as virtual switches to operate a machine based on simple on/off detection of touch force [3]. The fingernail sensors are also useful for robot teleoperation as well as acquiring human skills to train robots to perform complex assembly tasks [4]. Another application for fingertip touch force measurement using the fingernail sensor is a wearable replacement for a computer mouse [5], where the measured shear forces control the position or velocity of a pointer on a computer screen and the measured normal force controls the action of clicking.

Fingernail sensors have an analogous concept of operation to pulse oximeters which are used to measure pulse rate and oxygen saturation [6]. These devices estimate oxygenated and deoxygenated blood components based on their distinct light absorption coefficients by using LEDs of two wavelengths in the red to near-infrared region [7]. For the purpose of measuring the change of blood volume in the fingernail, commonly available LEDs of a wavelength of 770nm were used to remove the dependence of the light absorption coefficient of blood on oxygen saturation [1]. This wavelength is close to the "isobestic" wavelength of 800nm at which the absorption curves of oxygenated (HbO_2) and deoxygenated (Hb) blood intersect as shown in Figure 2.1.

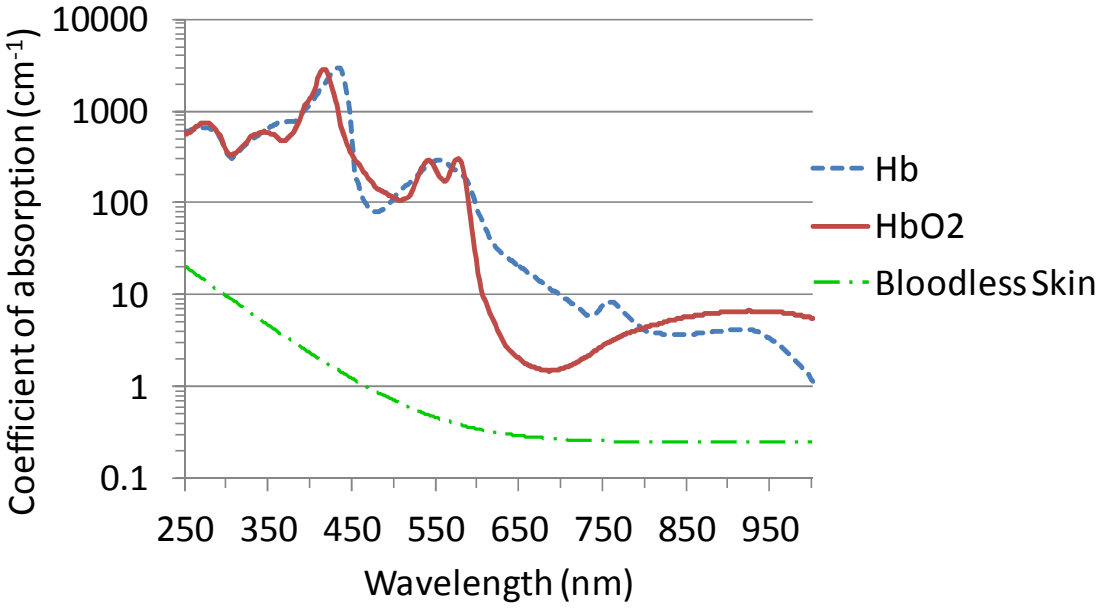

Figure 2.1 Absorption coefficients of skin perfused with oxygenated and deoxygenated blood as well as bloodless skin in the visible and near infrared spectra. This figure only shows approximate trends based on information from Scott Prahl [8] and Steven Jacques et al. [9].

In the visible range of light spectrum, the dependence on oxygen saturation is generally minimal below 600nm, Figure 2.1, where there are actually numerous isobestic wavelengths making this spectral region possibly useful for fingertip touch force detection using fingernail sensors.

The fingernail coloration patterns consist of red and white zones corresponding to increased and decreased blood volume in the nail bed, respectively. This implies that the change in light absorption of skin perfused with blood relative to bloodless skin is the key factor in distinguishing between these coloration patterns. In Figure 2.1, the main blood absorption bands are located between the wavelengths 400 and 425nm and the wavelengths 500 and 600nm, while at wavelengths longer than 600nm blood absorption is very low.

In the spectral region between 400 and 700nm, the main absorbers in skin are blood and melanosomes [10]. However, the concentration of melanosomes in the nail bed is unvarying and rather low; therefore its affect on the change of light absorption in the nail bed can be neglected. Keratin, which the fingernail is made of, almost exclusively absorbs UV radiation with a maximum approximately at 280nm and accordingly does not contribute to absorption of visible light [11].

In view of that, preliminary experiments were conducted with emitters of various wavelengths ranging between 470 and 660nm to select the wavelength which maximizes the distinguishability between the fingernail coloration zones. LEDs of wavelengths shorter than 470nm are not available in the desired surface mount packaging and therefore were not examined.

Preliminary results indicated that the fingernail coloration zones principally differ in their green component [12]. Additional experiments were conducted for a variety of light intensities at each wavelength to establish a linear relationship between the photodiode response and the incident light intensity. This did not only result in verifying the optimal wavelength but also quantified the transmittance change of the fingernail bed [13].

In the original fingernail sensor, the photodetectors were arranged in a laterally symmetric configuration over the fingernail area. The LEDs were located between the photodetectors such that each photodiode had at least one neighboring LED, resulting in an optoelectronic configuration which does not take into account the optimal separation distance between an LED/ photodiode pair. Hence, preliminary path length experiments were conducted at the optimal wavelength for a variety of light intensities, where separation distances of 2.5, 3.5, 4.5 and 6mm were tested. The minimum separation distance is limited by the size of the optoelectronic devices. Results indicated that the sensitivity of light transmittance to the optical path length is maximized when the surface mount LED and photodiode are placed as close together as possible [13].

In this paper, the optimal optical parameters for the transmittance of light through the human fingernail bed will be experimentally verified across a representative population of human subjects to ensure the repeatability of the obtained preliminary results. In the preliminary experiments, the optimal wavelength and path length were determined independently to minimize the experimental runs; however in this paper a fractional factorial design is implemented. The optimal optical parameters are determined based on the sensitivity and efficiency of light transmittance through the nail bed in a

statistically significant manner. Finally, important outcomes are discussed including light transmittance change through the fingernail bed, which varies as a function of applied force.

Experimental Design and Implementation

In order to enhance force prediction capabilities of the fingernail sensor, it is desired to optimize the performance of its optoelectronic devices by experimentally characterizing the sensitivity and efficiency of light transmittance through the nail bed to wavelength and optical path length. Hence, the experiments presented in this paper have been designed to serve this purpose.

Apparatus

Based on preliminary experiments, LEDs of wavelengths of 470, 525, 585, 610, and 660nm were selected to be placed on the fingernail and tested at separation distances of 2.5, 4.25 and 6mm from a photodiode of a wide spectral range (400-1100nm). Hence, 15 sensors of the different combinations of wavelengths and path lengths were assembled by bonding surface mount LEDs and photodetectors to printed circuit boards (PCBs) and attached to the fingernail via transparent double-sided adhesive tabs as shown in Figure 2.2. Given that the transmittance of light across the fingernail bed changes as a function of force applied to the fingertip, it is desired to experimentally determine the optimal optical parameters under varying force. Therefore, a three-axis force sensor, Figure 2.2, was placed beneath the fingertip to measure the applied normal and shear forces during each experiment. In order to ensure that the testing conditions do not change from one experiment to another, photodetectors were shielded to eliminate the ambient light effect.

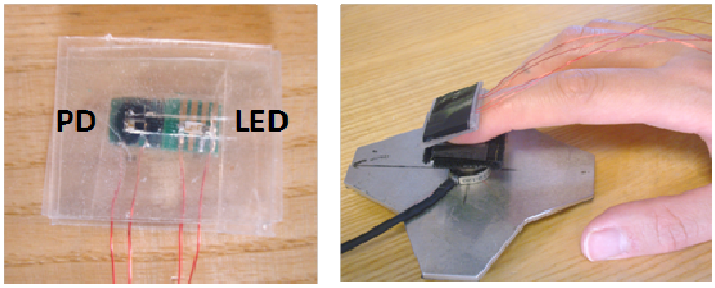

Figure 2.2 Experimental apparatus. To the left is an optoelectronic pair used to determine optimal optical parameters of light transmission through the nail bed. To the right is a three-axis force sensor placed beneath the fingertip to measure normal and shear forces.

A PC running LabVIEW and Matlab automatically selected the proper light intensity levels for each wavelength and provided visual feedback from the force sensor, placed beneath the fingertip, to help the human subject maintain the desired forces. Each photodiode signal was sampled at 10Hz using a data acquisition device along with LabVIEW at three different current levels supplied to the LED. The LED light intensity was held constant at each current level by using the transistor circuit demonstrated in Figure 2.3(a) [14]. The voltage to current converter shown in Figure 2.3(b) was implemented to produce a photodiode output voltage which is linearly proportional to the detected light intensity.

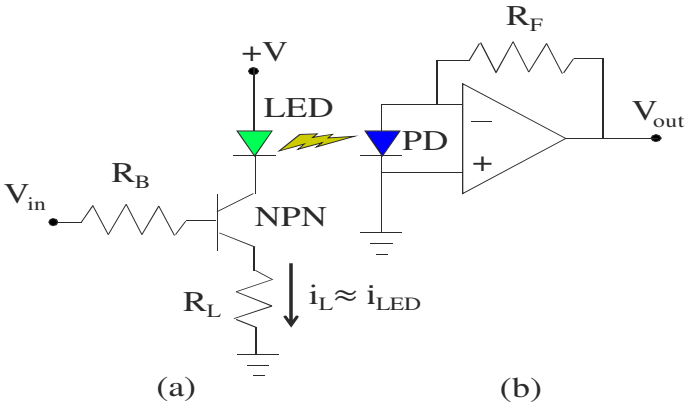

Figure 2.3 Plethysmograph circuitry. (a) LED current control circuitry and (b) linear response between photodiode voltage and LED light intensity.

Procedure

For the purpose of verifying the optimal optical parameters of light transmittance through the fingernail bed, 16 human subjects, 12 male and 4 female, completed 15 experiments each. To remove bias in the experiments, the order in which the various wavelengths were tested was randomized. Also at each wavelength, the order of the examined path lengths was unsystematic. The run time of each experiment was kept at 60 seconds to eliminate the fatigue factor.

A two-dimensional graphic user interface (GUI) was implemented to visually assist the test participants to alternate between two force poses in order to characterize the transmittance of light across the fingernail bed as a function of applied fingertip force. The two force poses shown in Figure 2.4 are chosen as it is fairly natural for the test participant to manually alternate between these poses. The nominal force pose corresponds to zero normal and shear forces while the $+F_y$ force pose corresponds to approximately -3N of normal force, +3N of longitudinal shear force, and zero lateral shear force. During each experiment, a sensor is mounted on the human subject's fingernail such that the optoelectronic (LED/PD) pair is located where the coloration zones change notably between the two desired force poses.

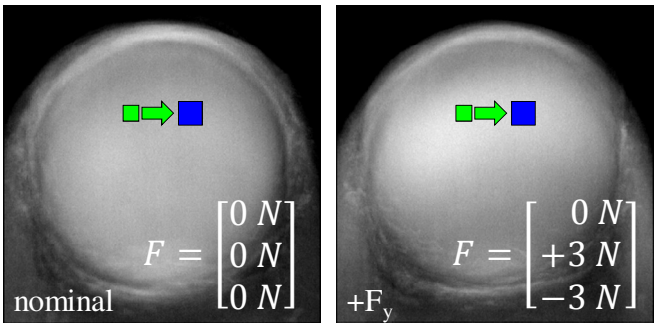

Figure 2.4 Desired force poses. Optoelectronic pair is placed where the coloration zone changes from red to white between nominal and $+F_y$ force poses, respectively.

Figure 2.5 illustrates the employed visual feedback. On the GUI two circles of distinct colors are displayed; the smaller red circle represents the actual applied force, measured by the force sensor placed beneath the fingertip, while the larger black circle represents the desired $+F_y$ force pose and is generated by the prompter. During each experiment, the test participant attempts to move his/her fingertip against the force-sensing platform such that the red circle moves back and forth between its initial position at the center of the GUI (nominal force pose) and the position of the black circle along the vertical axis, while matching the radius at each position. The three bars on the left side of the GUI provide an alternative visual feedback of the magnitude of the applied normal and shear forces measured by the force sensor. Particularly, the human subject attempts to approximately hold the fingertip lateral shear force at 0N, vary the longitudinal shear force from zero to +3N, and vary the normal force from zero to -3N.

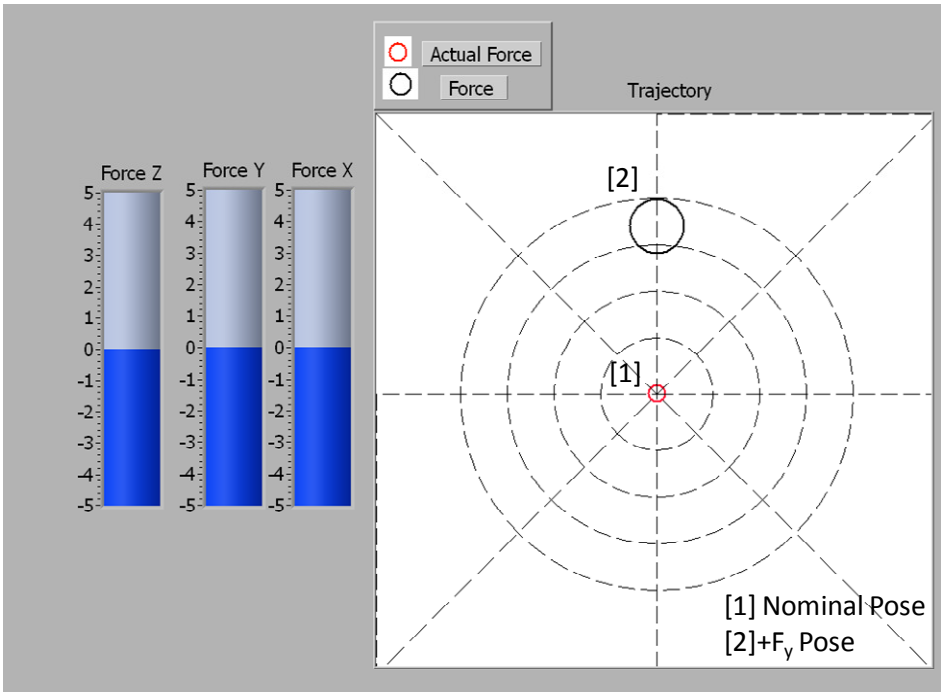

Figure 2.5 Graphic user interface. Visual feedback assists the test participants to alternate between the desired force poses.

In each experiment, one of the 15 sensors is mounted on the human subject's fingernail. Next, the test participant alternates between the desired force poses, while his/her fingertip is pressing against the force-sensing platform and the LED light intensity automatically changes between 3 different levels. The LED current levels are selected for a particular choice of wavelength via LabVIEW by strictly controlling the current supplied to the LED. This establishes a linear relationship between the photodiode response and the incident light intensity. At the end of each experiment, 3 data files corresponding to the 3 levels of LED light intensity are saved. Each file contains a record of time in seconds, the measured LED current i_{LED}, the sampled photodiode voltage V_{out}, and the normal and shear forces exerted on the fingertip and measured by the three-axis force sensor placed beneath the fingernail.

In Figure 2.6, sample force data, measured using the three-axis force sensor during an experiment, is demonstrated where the test participant alternates between the desired force poses previously shown in Figure 2.4. As shown, the applied lateral shear force was approximately held at 0N, the longitudinal shear force was varied from zero to +3N, and the normal force was varied from zero to -3N.

Figure 2.7 demonstrates sample test data of a photodiode placed on the fingernail at a separation distance of 2.5mm from a LED of a wavelength of 525nm. The photodiode signal was recorded at three various currents supplied to the LED corresponding to three distinct light intensities, while the test participant alternated between the two desired force poses. The peaks in Figures 2.7 approximately correspond to -3N normal force F_z, +3N longitudinal shear force F_y, and 0N lateral shear force F_x, while the valleys correspond to 0N normal and shear forces.

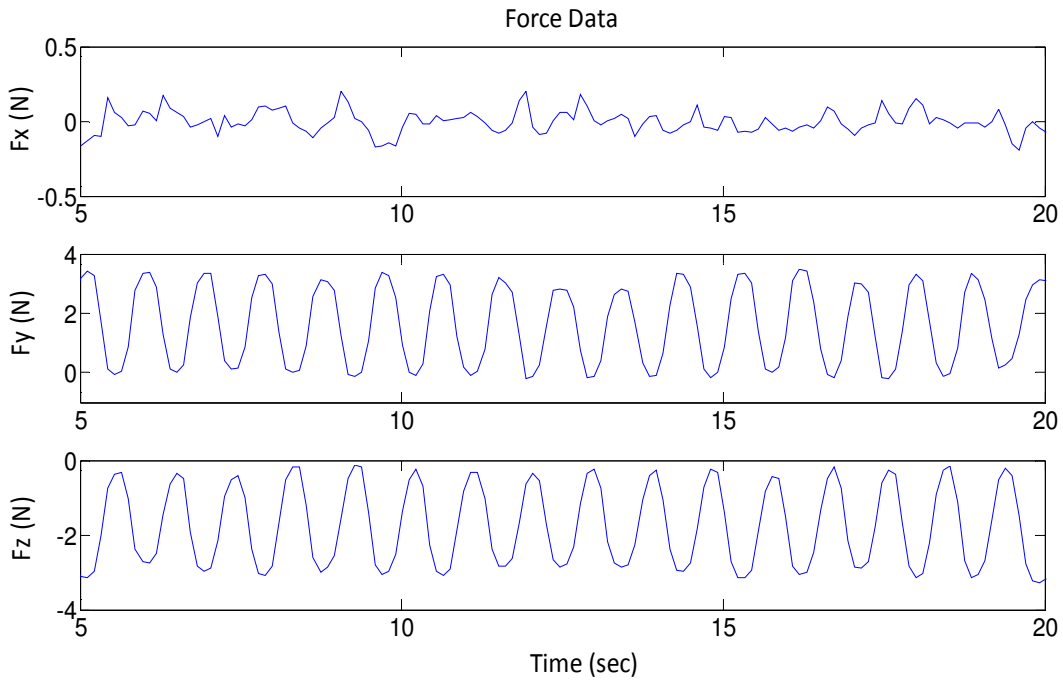

Figure 2.6 Sample force data. Normal and shear forces are measured using a three-axis force sensor placed beneath the fingertip.

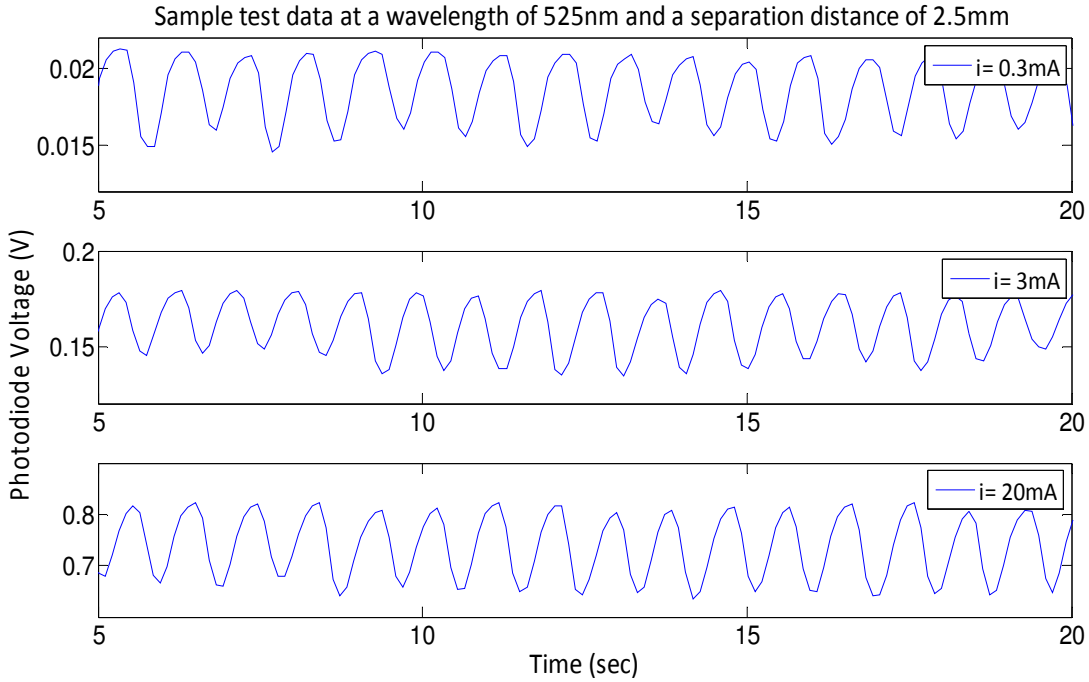

Figure 2.7 Sample test data under varying force. The signal of a photodiode placed on the fingernail at 2.5mm from a LED of a wavelength of 525nm is recorded at 3 different light intensities.

Results and Data Analysis

The analysis presented in this paper expands on the approach proposed by Abu-Khalaf and Mascaro in [13]. In this study, the optimal optical parameters for the transmittance of light through the human fingernail bed are determined by evaluating the sensitivity and efficiency of light transmittance to 15 different combinations of wavelength and optical path length for 16 human subjects.

From Figure 2.7, the following are computed at each light intensity level

$$\Delta V = \bar{V}_{PEAKS} - \bar{V}_{VALLEYS} \tag{2.1}$$

$$\bar{V} = (\bar{V}_{PEAKS} + \bar{V}_{VALLEYS})/2 \tag{2.2}$$

In (2.1), ΔV is the change in the photodiode voltage resulting from the variation in blood volume beneath the fingernail when forces are applied on the fingertip. Since the variations in the photodiode voltage at the peaks and the valleys are minimal, ΔV is calculated by taking the difference between the mean of the voltages at the peaks and that at the valleys. In (2.2), $\bar{V}$ is the median photodiode voltage.

To find the sensitivity of light transmittance through the nail bed to a specific wavelength and path length, the change in the photodiode voltage ΔV is plotted versus the median voltage $\bar{V}$ at the 3 different intensity levels as shown in Figure 2.8. The slope of the best fit line corresponds to the sensitivity of light transmittance of the fingernail bed to a wavelength of 525nm and a path length of 2.5mm. Likewise, the responsive efficiency of plethysmography E_{SENSOR} can be found by plotting ΔV versus the 3 LED current levels as shown in Figure 2.9.

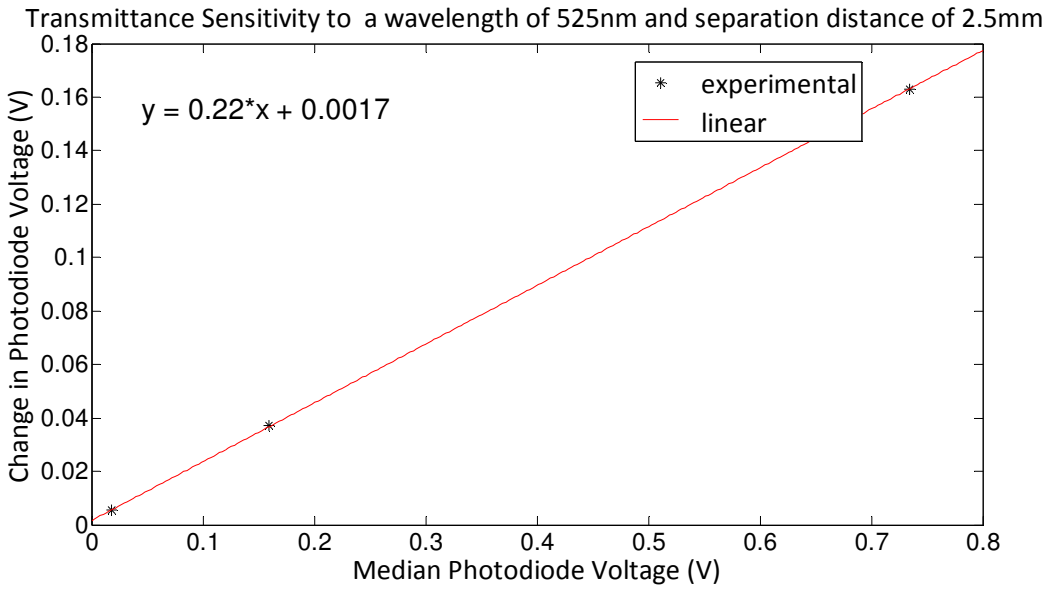

Figure 2.8 Sensitivity of light transmittance through the nail bed. Slope ($\Delta V/\bar{V}$) corresponds to sensitivity to a wavelength of 525nm and a path length of 2.5mm.

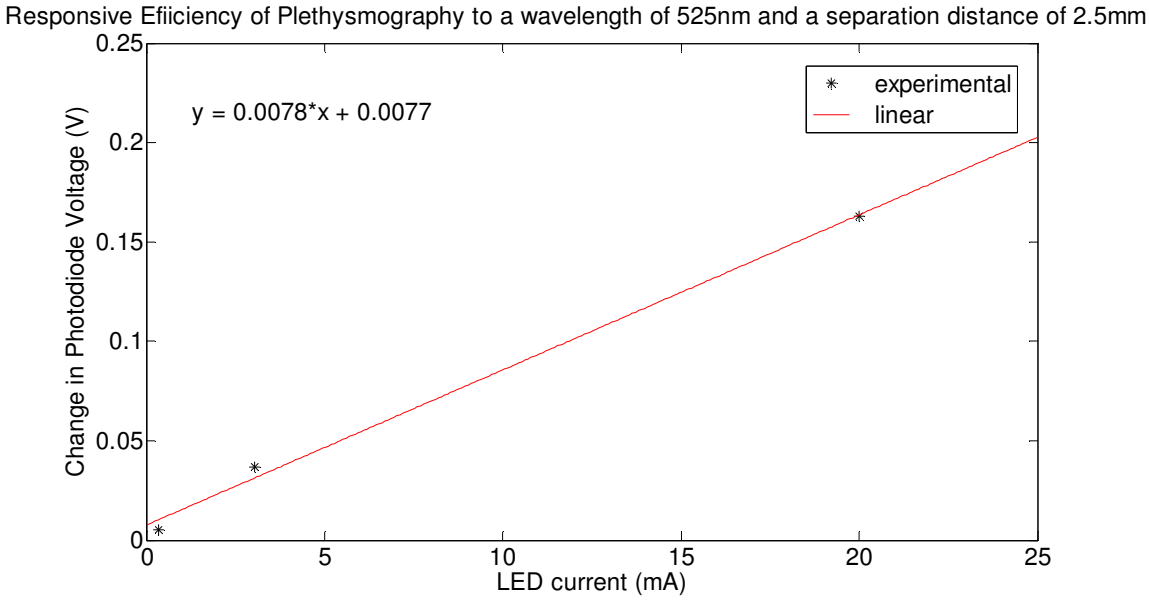

Figure 2.9 Responsive efficiency of plethysmography. Slope ($\Delta V/ i_{LED}$) corresponds to efficiency at wavelength of 525nm and a path length of 2.5mm.

In Figure 2.8, an increased slope $\Delta V / \bar{V}$ yields better sensitivity of the fingernail coloration patterns to a specific wavelength and path length combination; as it indicates a larger change in the photodiode signal to the varying force exerted on the fingertip. Similarly, in Figure 2.9 an increased slope $\Delta V / i_{LED}$ yields better responsive efficiency of plethysmography as an efficient combination of wavelength and path length results in a larger change in the photodiode voltage for the same supplied LED current.

Statistical Analysis

In order to evaluate the optimal wavelength and path length for the transmittance of light through the human fingernail bed in a statistically significant manner, the average and standard deviation of sensitivity and efficiency of light transmittance at each of the 15 combinations of wavelengths and path lengths are computed across all subjects.

In Figure 2.10, the average sensitivity of light transmittance through the nail bed is plotted at each of the 15 examined combinations of wavelengths and path lengths with error bars corresponding to the standard deviations. The general trends indicate that voltage change given our choice of photodiode is relatively small for orange and red wavelengths (610nm and 660nm, respectively). On the other hand, sensitivity is not significantly better at one path length versus the other.

In Figure 2.11, the average responsive efficiency of plethysmography is plotted at each of the 15 examined combinations of wavelengths and path lengths with error bars corresponding to the standard deviations. The yellow and red wavelengths (585nm and 660nm, respectively) are noticeably the least efficient, while the shortest path length (2.5mm) apparently yields the largest voltage change per unit of consumed energy.

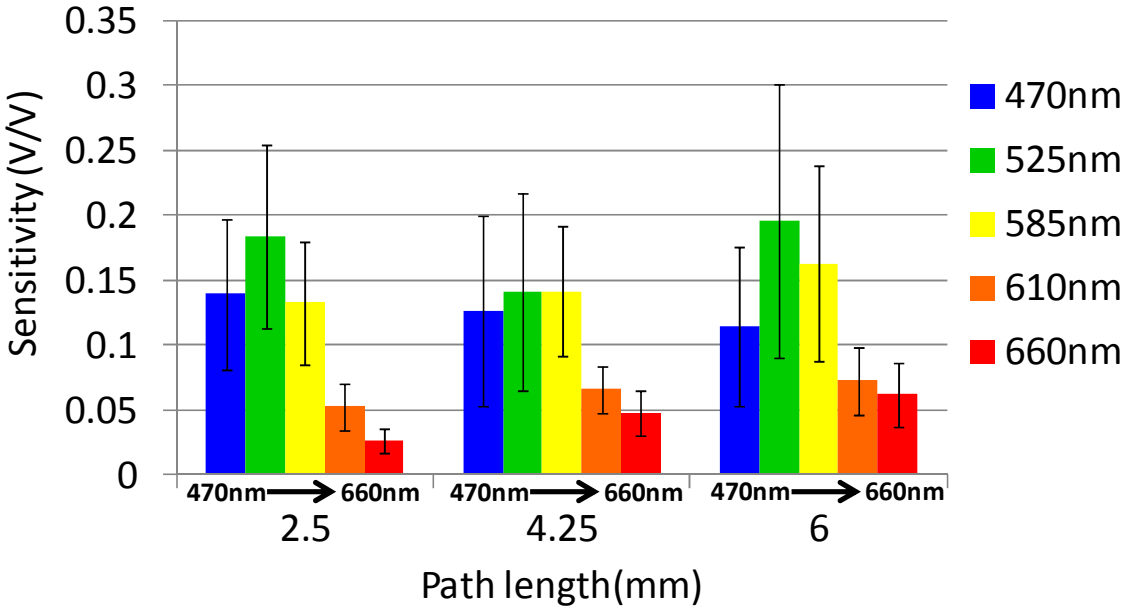

Figure 2.10 Average sensitivity of light transmittance through the nail bed to wavelength and path length. Data for 16 human subjects were averaged and plotted with error bars corresponding to the standard deviations.

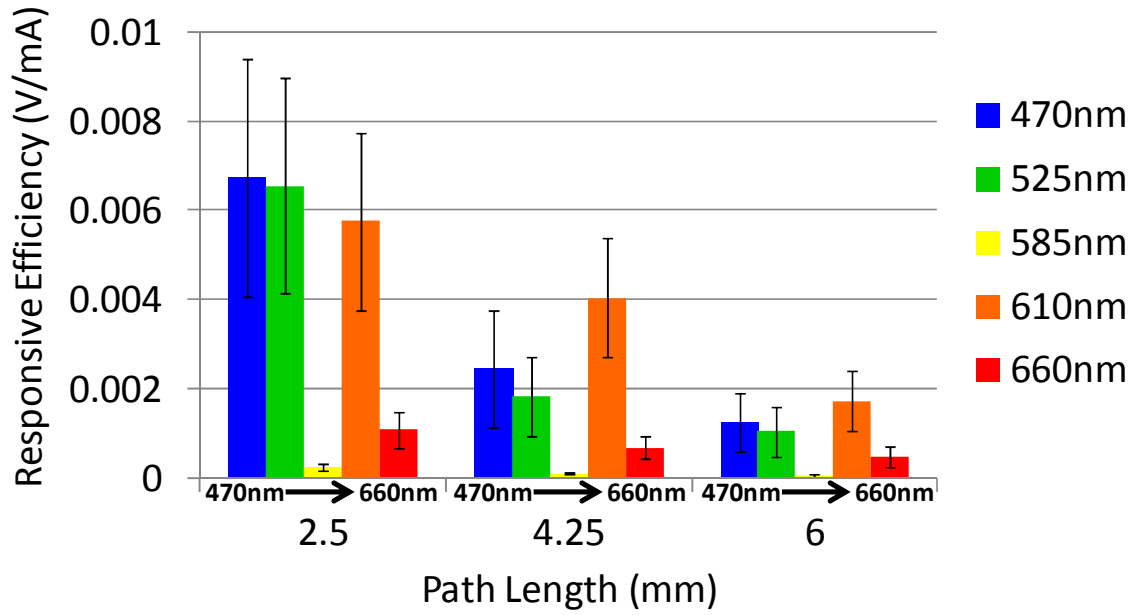

Figure 2.11 Average responsive efficiency of plethysmography to wavelength and path length. Data for 16 human subjects were averaged and plotted with error bars corresponding to the standard deviations.

To verify the optimal wavelength and path length in a statistically significant manner, firstly, it is chosen to establish that wavelengths of 585nm, 610nm, and 660nm are not optimal. Secondly, the path lengths are examined to verify the optimal path length. Thirdly, the remaining wavelengths (470nm and 525nm) are assessed at the optimal path length to determine the optimal wavelength.

This requires performing a hypothesis test to compare the means of the different combinations of wavelength and path length in Figures 2.10 and 2.11. Let μ_1 and μ_2 represent the mean responsive efficiency to 660nm at 2.5mm and 470nm at 2.5mm, respectively. Then, the statistical hypotheses are

H_o: $\mu_1 = \mu_2$ (mean responsive efficiency to 660nm at 2.5mm is not smaller)

H_1: $\mu_1 < \mu_2$ (mean responsive efficiency to 470nm at 2.5mm is greater)

Mann-Whitney *U* test is performed to evaluate the statistical significance of one combination of wavelength and path length over another as it does not require normal distribution of the variable under consideration [15]. This nonparametric test requires ranking the data from the 16 human subjects such that data of the two compared combinations are grouped and sorted in an ascending manner. The smallest quantity is given the rank of 1 while the largest quantity is given the rank of $Ns = 32$. When two or more quantities are tied, each is assigned the mean of the ranks they would have been assigned if they were not tied.

Table 2.1 shows responsive efficiency data for 16 human subjects to 660nm at 2.5mm and 470nm at 2.5mm. All data from both samples are combined and ranked from smallest to largest, and the sum of the overall ranks for each of the combinations A_1 and A_2 is computed.

Table 2.1 Results of ranking responsive efficiency data for 16 human subjects to 660nm at 2.5mm (A_1) and 470nm at 2.5mm (A_2).

Responsive Efficiency to 660nm at 2.5mm (A_1)	Overall Rank	Responsive Efficiency to 470nm at 2.5mm (A_2)	Overall Rank
0.0007	3	0.0018	16.5
0.0007	3	0.0035	18
0.0007	3	0.0045	19
0.0007	3	0.0048	20.5
0.0007	3	0.0048	20.5
0.0008	6.5	0.005	22
0.0008	6.5	0.0067	23
0.0009	8	0.0069	24
0.0011	9	0.007	25
0.0012	10.5	0.0071	26.5
0.0012	10.5	0.0071	26.5
0.0013	12	0.0082	28.5
0.0015	13	0.0082	28.5
0.0016	14	0.0095	30
0.0017	15	0.0113	31
0.0018	16.5	0.0115	32
	$\Sigma R_{A1} = 136.5$		$\Sigma R_{A2} = 391.5$

The U statistic is the number of times the rank of a quantity in one combination (A_1) precedes the rank of a quantity in the other combination (A_2), where the value for the U observed on combination A_1 is given by [15]:

$$U_{A1obs} = n_{A1}n_{A2} + \frac{n_{A1}(n_{A1}+1)}{2} - \sum R_{A1} \tag{2.3}$$

where n_{A1} = number of data points in combination A_1

n_{A2} = number of data points in combination A_2

ΣR_{A1} = sum of the ranks assigned to data points in combination A_1

Similarly,

$$U_{A2obs} = n_{A1}n_{A2} + \frac{n_{A2}(n_{A2}+1)}{2} - \sum R_{A2} \tag{2.4}$$

where $n_{A1} = n_{A2} = 16$ and ΣR_{A2} is the sum of the ranks assigned to data points in combination A_2. Substituting values into equations 2.3 and 2.4 results in $U_{A1obs} = 255.5$ and $U_{A2obs} = 0.5$. The smaller of the two values of U_{obs} is compared to the critical values of U in the Mann-Whitney U test tables.

For $n_{A1} = n_{A2} = 16$, $U_{crit} = 75$ at the 95% significance level ($\alpha = 0.05$) and $U_{crit} = 60$ at the 99% significance level ($\alpha = 0.01$). A value of the smaller U_{obs} which is equal or less than U_{crit} is statistically significant and falls in the rejection region; H_o is rejected and H_1 is accepted. For the specific example introduced here, U_{A2obs} is less than U_{crit} at the 99% significance level and accordingly the mean responsive efficiency to 470nm at 2.5mm is significantly greater than that to 660nm at 2.5mm.

The maximum average responsive efficiency of plethysmography to yellow wavelength (585nm) and that to red wavelength (660nm) are located at 2.5mm. To establish that these wavelengths are significantly less efficient than blue, green, and orange wavelengths at 2.5mm, the smaller U_{obs} values for the combinations of interest are computed using equations (2.3) and (2.4) and tabulated in Table 2.2. All U_{obs} values are less than the critical value of U at the 99% significance level ($U_{crit} = 60$). Hence, yellow and red wavelengths are found to be significantly less efficient than blue, green, and orange wavelengths at 2.5mm with a 99% significance level and accordingly are not optimal.

Table 2.2 Statistical significance of responsive efficiency of plethysmography to 585nm and 660nm. Yellow and red wavelengths are significantly worse than blue, green, and orange wavelengths at 2.5mm.

Responsive Efficiency at 2.5mm (A_1)	Responsive Efficiency to 470nm at 2.5mm (A_2)	Responsive Efficiency to 525nm at 2.5mm (A_2)	Responsive Efficiency to 610nm at 2.5mm (A_2)
Responsive Efficiency to 660nm	$U_{obs} = 0.5$	$U_{obs} = 0$	$U_{obs} = 0$
Responsive Efficiency to 585nm	$U_{obs} = 0$	$U_{obs} = 0$	$U_{obs} = 0$

Next, the maximum average sensitivity of light transmittance through the nail bed to 610nm, which is located at 6mm, is compared to the sensitivity to the remaining wavelengths at all path lengths. Figure 2.12 plots the *U*-values for the examined combinations and the most conservative significance levels. All U_{obs} values are less than the critical value of *U* at the 95% significance level (U_{crit} = 75). Accordingly, the maximum transmittance sensitivity to orange is found to be significantly worse and the wavelength of 610nm is not optimal.

It is desired to evaluate the optimal path length at each of the remaining blue and green wavelengths. When inspecting the average transmittance sensitivities, Figure 2.10, it appears that sensitivity is not significantly better at one path length versus the other. To verify this assessment, *U*-values are computed to compare the 3 examined path lengths at each wavelength and are plotted in Figure 2.13. Evidently, the optimal path length cannot be determined from the average transmittance sensitivities as all U_{obs} values are considerably larger than the critical value of *U* at the 95% significance level (U_{crit} = 75).

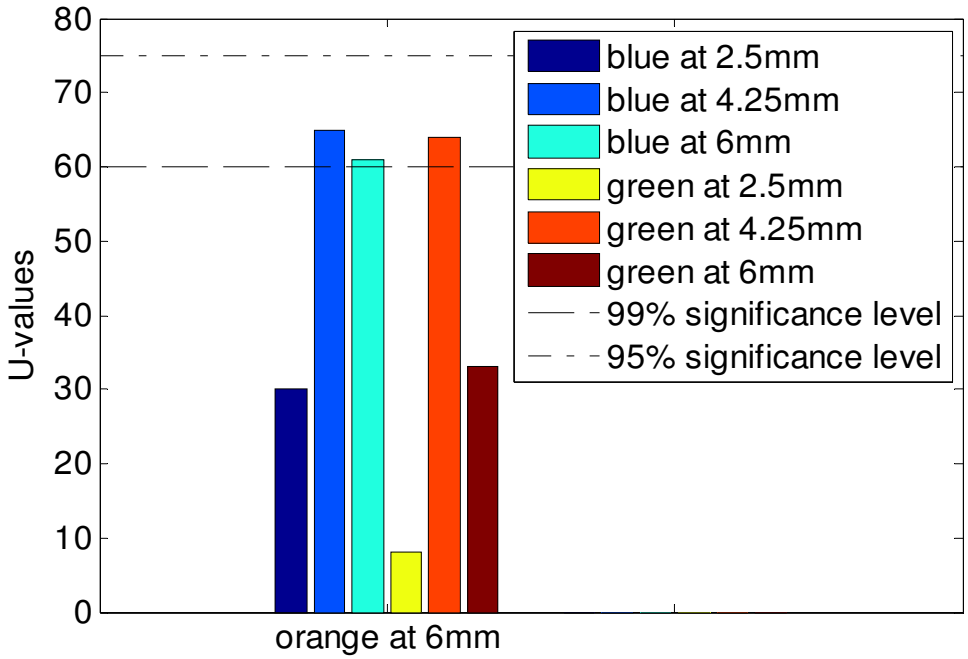

Figure 2.12 Statistical significance of sensitivity of light transmittance through the nail bed to 610nm. Orange is significantly worse than blue and green.

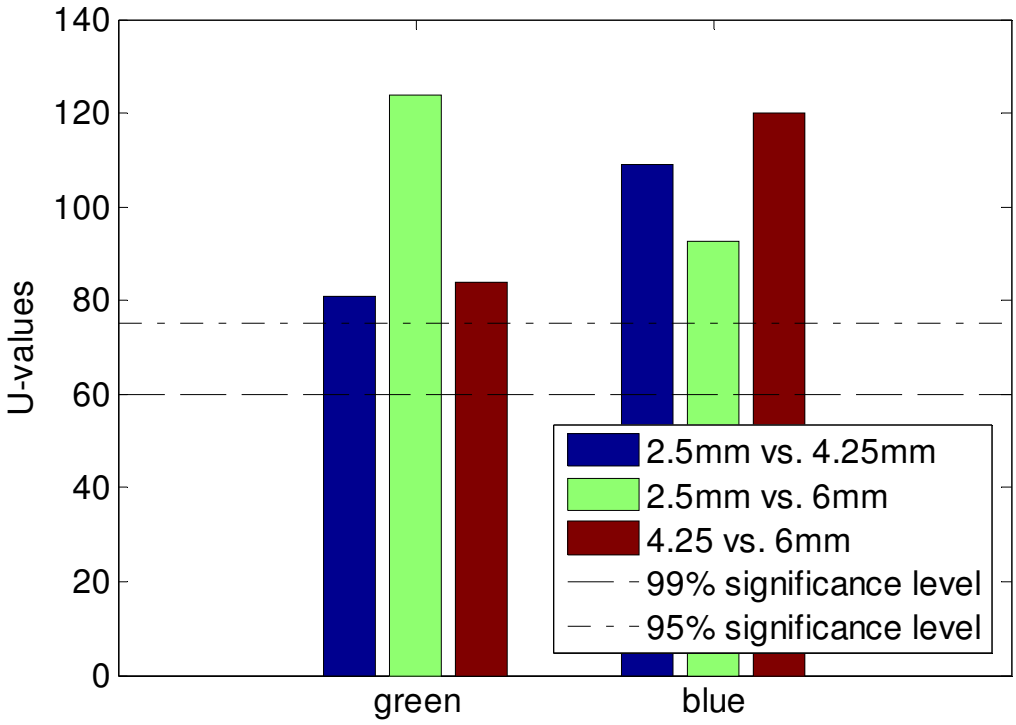

Figure 2.13 Statistical significance of sensitivity of light transmittance through the nail bed to path length. Sensitivity is not significantly better at one path length versus the other.

Subsequently, the average responsive efficiency of plethysmography, Figure 2.11, is inspected in order to determine the optimal path length at each of the remaining wavelengths. Table 2.3 demonstrates the *U*-values for the combinations of interest, where the 3 examined path lengths are compared at each wavelength. At both the green and blue wavelengths, a path length of 2.5mm is found to be significantly optimal since all U_{obs} values are less than the critical value of *U* at the 99% significance level (U_{crit} = 60).

After verifying the optimal path length, the remaining blue and green wavelengths, 470nm and 525nm, respectively, are examined to determine the optimal wavelength. While the average responsive efficiencies of plethysmography at the two wavelengths are not explicitly distinguishable, the average sensitivities of light transmittance demonstrate that the green wavelength is optimal at 2.5mm. To verify this statement in a statistically significant manner, a normal approximation of *U* is used as the tables for critical values of *U* are only available for the most conservative significance levels.

Table 2.3 Statistical significance of responsive efficiency of plethysmography to path length. The shortest path length of 2.5mm is significantly optimal at 525nm and 470nm.

	Responsive Efficiency at 2.5mm (A_1) vs. 4.25mm (A_2)	Responsive Efficiency at 2.5mm (A_1) vs. 6mm (A_2)	Responsive Efficiency at 4.25mm (A_1) vs. 6mm (A_2)
Responsive Efficiency to 525nm	$U_{obs} = 0$	$U_{obs} = 0$	$U_{obs} = 58.5$
Responsive Efficiency to 470nm	$U_{obs} = 17$	$U_{obs} = 3.5$	$U_{obs} = 55.5$

U is approximately normally distributed for $n_1 \geq 8$ and $n_2 \geq 8$. Accordingly, the standard variable is given by [16]

$$z = \frac{U - \mu_U}{\sigma_U} = \frac{U - (n_1 n_2)/2}{\sqrt{n_1 n_2 (n_1 + n_2 + 1)/12}} \tag{2.5}$$

where U is the smaller of the two values of U_{obs}, computed using equations (2.3) and (2.4), and is found to be equal to 79. The z-table can be used to statistically test the difference between the responsive efficiency to the green wavelength and that to the blue wavelength at 2.5mm [17]. If the absolute value of the calculated z is larger or equal to the tabulated z value, the hull hypothesis H_o is rejected. For $n_1 = n_2 = 16$, |calculated z| = 1.847 and the |tabulated z| = 1.77, thus the green wavelength is optimal at the optimal wavelength.

Discussion

The preceding results serve as strong evidence that the optical parameters for the transmittance of light through the human fingernail bed are optimized when using green light (525nm) and when the surface mount LED and photodiode are placed as close together as possible (2.5mm). The optimal optical parameters successfully verify the preliminary results from [12] and [13], and also agree with the absorption coefficients of skin, shown in Figure 2.1, where the optimal wavelength is located in one of the two main blood absorption bands between the wavelengths 500 and 600nm.

In relevant work, Sun, Hollerbach and Mascaro [18], used an external camera system to image the fingernail and surrounding skin for fingertip touch force

measurement. The green channel of the camera's Red, Green, and Blue (RGB) color space was used as it was found to result in better coloration response as well as linearity to applied fingertip force when compared to the other channels. This also supports the experimental results introduced in this paper, which quantitatively determined the optimal wavelength. Incorporating the optimal optical parameters in the design of the fingernail sensor is anticipated to result in optimized detection of blood volume variations beneath the fingernail, which is directly related to touch forces exerted on the fingertip.

Another quantity that is worth characterizing is the transmittance change of the fingernail bed ΔT_{FB} for the various wavelength and path length combinations, while alternating between the two poses shown in Figure 2.4. Though this is not necessary to verify the optimal optical parameters, it satisfies a scientific curiosity of identifying light transmittance through the fingernail bed as a function of force. It is also expected to contribute in constructing a realistic model of light transmittance through the nail bed. ΔT_{FB} can be computed for a specific wavelength λ and path length d as follows

$$E_{SENSOR}(\lambda, d) = E_{LED}(\lambda)\Delta T_{FB}(\lambda, d)R_{PD}(\lambda) \tag{2.6}$$

where $\Delta T_{FB}(\lambda,\ d)$ is in steradians (sr), $E_{SENSOR}(\lambda,\ d)$ is the responsive efficiency of plethysmography in V/mA, $E_{LED}\ (\lambda)$ is the radiant efficiency of the LED in mW/sr·mA, and $R_{PD}\ (\lambda)$ is the amplified responsivity of the photodiode in V/W.

As previously shown in Figure 2.9, $E_{SENSOR}(\lambda,\ d)$ is an indicator of voltage change per unit of consumed energy ($\Delta V/\ i_{LED}$) for available battery voltage, and can be found by plotting the change in photodiode voltage versus the 3 LED current levels at a designated

wavelength and path length combination. The radiant efficiency $E_{LED}(\lambda)$ is a measure of the emitted power to input power for available battery voltage and is defined as the ratio of LED radiant intensity $I_e(\lambda)$ in mW/sr to LED forward current $i_f(\lambda)$ in mA. The radiant intensity $I_e(\lambda)$ can be expressed in terms of the LED luminous intensity $I_v(\lambda)$ in mcd (millicandela) and the LED dimensionless luminous efficiency $V(\lambda)$ [19]. Hence the radiant efficiency can be evaluated from the following equation

$$E_{LED}(\lambda) = \frac{\mathrm{I_e}(\lambda)}{\mathrm{i_f}(\lambda)} = \frac{\mathrm{I_v}(\lambda)}{(683)\mathrm{V}(\lambda)\mathrm{i_f}(\lambda)} \tag{2.7}$$

Each examined LED has an explicit luminous intensity and forward current specified in its datasheet. The luminous efficiency for each wavelength is determined based on the spectral luminous efficiency data from Pedrotti and Pedrotti [19]. Figure 2.14 demonstrates the radiant efficiency in mW/sr·mA computed for our choice of examined LEDs.

Figure 2.15 shows the amplified responsivity of the photodiode $R_{PD}(\lambda)$ in V/W which is computed from equation (2.8), where R_F is the feedback resistance in Ω, shown in Figure 2.3(b), and R(λ) is the responsivity of photodiode in A/W from the spectral of our choice of photodiode.

$$\mathrm{R_{PD}}(\lambda) = [\mathrm{R}(\lambda)][\mathrm{R_F}] \tag{2.8}$$

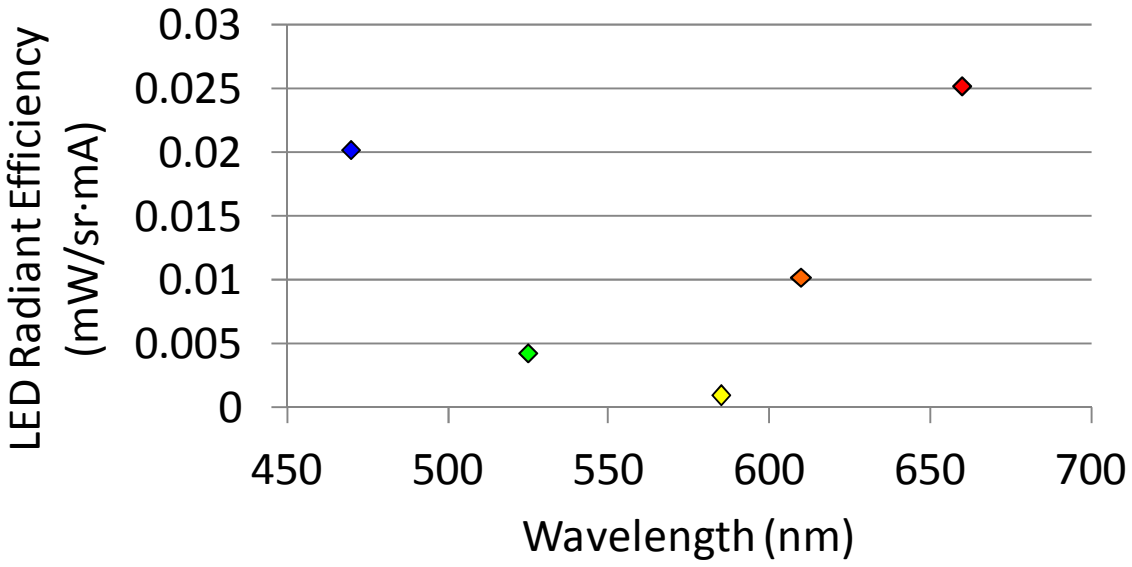

Figure 2.14 LED radiant efficiency in mW/sr·mA to various examined LEDs.

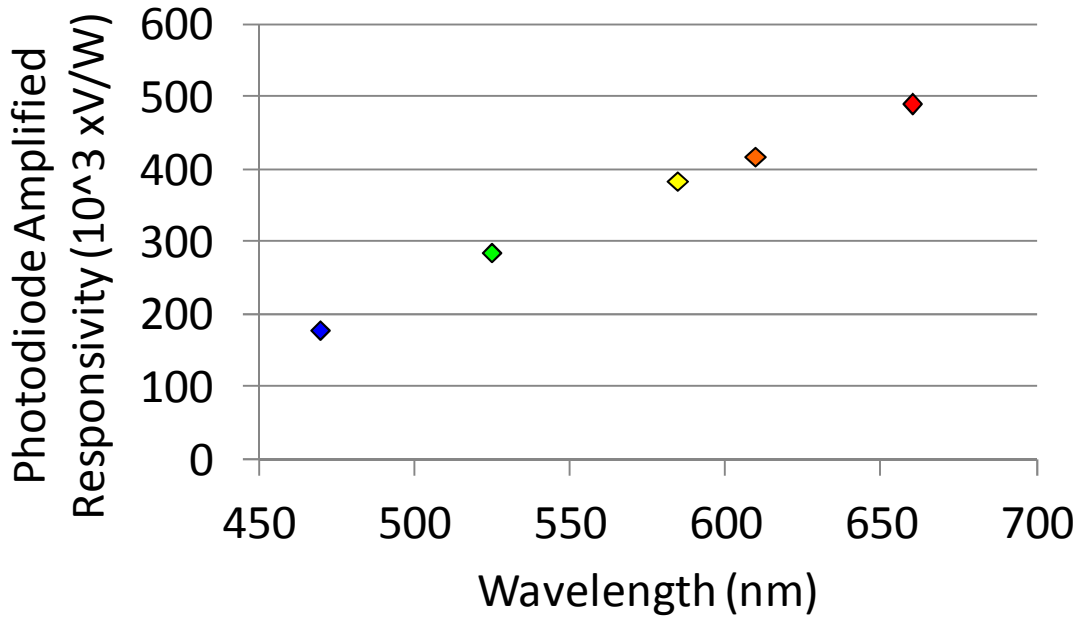

Figure 2.15 Photodiode amplified responsivity in (10^3)×V/W to various examined wavelengths.

Subsequently, the change in light transmittance through the nail bed as a function of force is computed from equation (2.6) for all 16 human subjects at each of the 15 examined combinations of wavelengths and path lengths. The results are averaged and plotted in Figure 2.16 with error bars corresponding to the standard deviations.

It is evident that light transmittance change in the fingernail bed marks the green wavelength at a separation distance of 2.5mm as a clear winner. This implies that if LED efficiency and photodiode responsivity were equal at all wavelengths, green would be a clear design choice. However, blue LEDs are 5x more efficient than green in terms of mW/sr·A, as shown in Figure 2.14, while the photodiode is 2/3 as sensitive at blue than green as demonstrated in Figure 2.15. Accordingly, blue LEDs have a net advantage of x3 compared to green LEDs (at least for our choice of LEDs and photodiode) which almost cancels out the x3 light transmittance change advantage of green over blue.

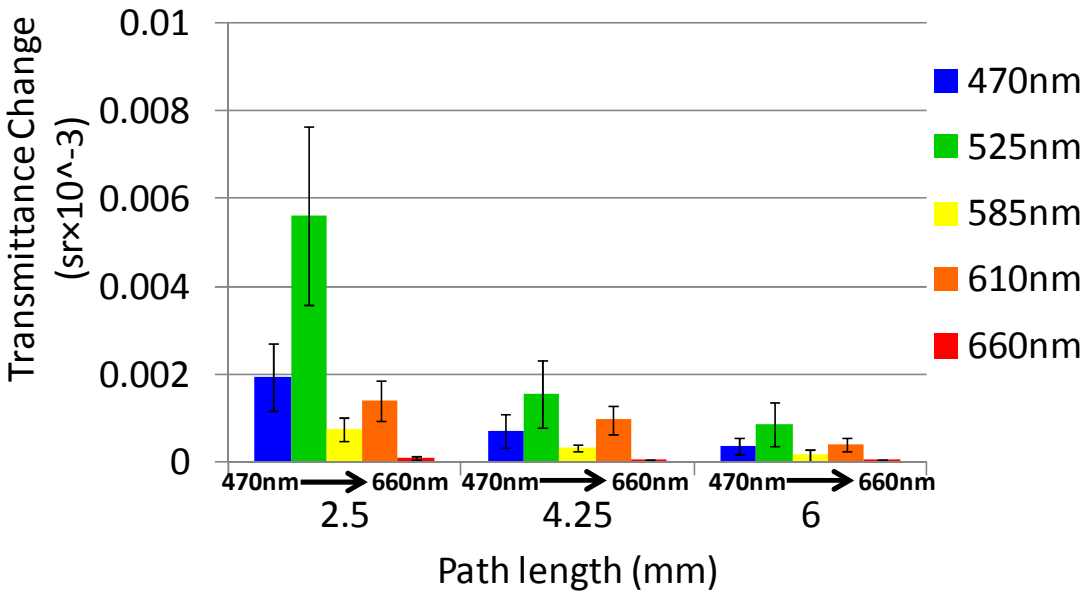

Figure 2.16 Average light transmittance change through the nail bed to wavelength and path length. Data for 16 human subjects were averaged and plotted with error bars corresponding to the standard deviations.

Conclusion

In this paper, the optimal optical parameters for light transmittance through the human fingernail bed have been experimentally determined in order to optimize detection of blood volume variations in the nail bed, which vary as a function of applied force. The sensitivity and efficiency of light transmittance to wavelength and optical path length have been thoroughly investigated. Results verify that the optical parameters are optimized when using a green light (525nm) and when the surface mount LED and photodiode are placed as close together as possible (2.5mm).

The light transmittance change of the fingernail bed has been also characterized for a variety of wavelength and path length combinations under varying force. Though results do not explicitly identify green as the optimal wavelength, they mark both green and blue wavelengths as top contenders. On the other hand, results suggest that a path length of 2.5mm is optimal in terms of light transmittance change.

In future work, experimental data of light transmittance change are anticipated to contribute in constructing a physically-based model of light transmittance through the nail bed. Subsequently, the optical model will allow for optimizing the arrangement of LEDs and photodetectors on the nail surface by incorporating the optimal path length. Ultimately, the optimization of the optoelectronic configuration, along with using the optimal wavelength, is expected to enhance the force sensor prediction capabilities.

References

[1] S. Mascaro and H. Asada, “Photoplethysmograph fingernail sensors for measuring finger forces without haptic obstruction,” *IEEE Trans. on Robotics and Automation*, vol. 17, no. 5, pp. 698–708, 2001.

[2] S. Mascaro and H. Asada, "The common patterns of blood perfusion in the fingernail bed subject to fingertip touch force and finger posture," *Haptics-e: The Electronic Journal of Haptics Research*, vol. 4, no. 3, pp. 1-6, 2006.

[3] S. Mascaro and H. Asada, "Virtual switch human-machine interface using fingernail touch sensors," *Proc. IEEE Int. Conf. Robotics and Automation*, vol. 4, pp. 2533-2538, 1999.

[4] S. Mascaro, S., K.W. Chang, and H. Asada, "Finger touch sensors using instrumented nails and their application to human-robot interactive control," *Proc. ASME Dynamic Systems and Control Division*, vol. 64, pp. 91-96, 1998.

[5] S. Mascaro and H. Asada, "Measurement of finger posture and three-axis fingertip touch force using fingernail sensors," *IEEE Trans. on Robotics and Automation*, vol. 20, no. 1, pp. 26-35, 2004.

[6] Y. Mendelson and B.D. Ochs, "Noninvasive pulse oximetry utilizing skin reflectance photoplethysmography," *IEEE Transactions on Biomedical Engineering*, vol. 35, no. 10, pp. 798-805, 1988.

[7] K. K. Tremper and S. J. Barker, "Pulse oximetery," *Anesthesiology*, vol.70, no. 1, pp. 98–108, 1989.

[8] S. Prahl, "Tabulated molar extinction coefficient for hemoglobin in water," http://omlc.ogi.edu/spectra/ hemoglobin/summary.html, March, 1998.

[9] M.J.C. Van Gemert, S.L. Jacques, H.J.C.M. Sterenborg, W.M. Star, "Skin optics," *IEEE Transactions on Biomedical Engineering*, vol.36, issue 12, pp. 1146-1154, 1989.

[10] R.R. Anderson and J.A. Parrish, "The optics of human skin," *Journal of Investigative Dermatology*, vol. 77, no. 1, pp. 13-19, 1981.

[11] K.P. Nielsen, L. Zhao, J.J. Stamnes, K. Stamnes, and J. Moan, "The optics of human skin: Aspects important for human health," *The Norwegian Academy of Science and Letters: Solar Radiation and Human Health*, pp. 35-46. 2008.

[12] J. Abu-Khalaf and S. Mascaro, "Optimization of fingernail sensor design based on fingernail imaging," *Proceedings of the SPIE Novel Optical Systems Design and Optimization XIII*, vol. 7787, 8 pages, 2010.

[13] J. Abu-Khalaf and S. Mascaro, "Optimization of fingernail sensing technique based on optical experimentation and modeling," *Proceedings of the IEEE Sensors Applications Symposium (SAS)*, pp. 283-288, 2011.

[14] P. Scherz, Practical Electronics for Inventors. New York, NY: McGraw-Hill, 2nd edition, 2007.

[15] H. O. Kiess, Statistical Concepts for the Behavioral Sciences. Needham Heights, MA: Allyn & Bacon, 2nd edition, 1996.

[16] Nadim Nachar, "The Mann-Whitney U: A test for assessing whether two independent samples come from the same distribution," *Tutorials in Quantitative Methods for Psychology*, vol. 4(1), pp. 13-20, 2008.

[17] N. Weiss and M. Hassett, Introductory Statistics. Addison-Wesley Publishing Company, Inc., 6th edition, 2002.

[18] Y. Sun, J. Hollerbach, and S. Mascaro, "Estimation of Finger Force Direction with Computer Vision," *IEEE Transactions on Robotics*, vol. 25, no. 6, pp. 1356-1369, 2009.

[19] F. L. Pedrotti and L. S. Pedrotti, Introduction to Optics. Englewood Cliffs, NJ: Prentice-Hall, Inc., 1987.

CHAPTER 3

OPTIMIZATION OF FINGERTIP FORCE DIRECTION ESTIMATION BASED ON OPTICAL MODELING AND EXPERIMENTATION

Abstract

This paper describes the optimization of fingernail sensors for detecting fingertip touch force direction which has several applications in the area of human-machine interaction. The fingernail sensor uses optical reflectance photoplethysmography to measure the change in blood perfusion in the fingernail bed when the finger pad touches a surface with various forces. In the original fingernail sensor, color changes observed through the fingernail have been measured by mounting an array of 6 LEDs and 8 photodetectors on the fingernail in a laterally symmetric configuration. The optical components were located such that each photodiode had at least one neighboring LED. The role of each of the photodetectors was investigated in terms of the effect of removing one or more photodetectors on force prediction estimation. The analysis suggested designing the next generation of fingernail sensors with less than eight photodetectors. This paper proposes an optimal redesign by introducing an optical model that describes light transmittance between an LED and a photodiode in the fingernail area based on optical experimentation. Using this model, the optimal locations of the optoelectronic

devices are predicted by analyzing a photographic catalog composed of six different force poses, which represent average fingernail coloration patterns of 15 human subjects. The resulting optimal optoelectronic configuration is validated by examining its ability to classify the correct force direction of test images of 15 human subjects. With individual training, the overall classification accuracy was 97%. A reduced configuration is derived from the optimal optoelectronic locations in order to facilitate the fabrication of the optimized fingernail sensor without significantly compromising the classification accuracy.

Introduction

Measurement of fingertip touch forces plays a key role in the fields of haptics, robotics and virtual reality [1]. In particular, it has several applications in the area of human-machine interaction, such as operating a machine using virtual switches based on simple on/off detection of touch force [2]. It is also useful for robot teleoperation and acquiring human skills to train robots to perform complex assembly tasks [3, 4]. In addition, it contributes to the study of human grasping and manipulation as well as characterizing the human haptic sense [5, 6].

Typically, normal and shear forces acting on the fingertips have been measured using electronic gloves with force-sensing pads [7]. However, this method was found to have an undesirable effect on the human haptic sense as it forms a barrier between the human fingers and the surrounding environment. In previous work, Mascaro and Asada proposed a new sensing approach which allows for full range of haptic sense by mounting optical reflectance photo-plethysmograph sensors on the fingernail [8]. In their work, they also established that distinct patterns of color changes occur along the

fingernail area as the fingertip is pressed down against a planar surface [9]. The pattern of observable color changes is directly related to changes in the blood volume in the nail bed, which varies as a function of applied force, and allows for fingertip force detection without haptic obstruction.

Calibration experiments were performed to train and validate a linear predictor for 7 human subjects, based on readings from the fingernail sensor array of 6 LEDs and 8 photodetectors [10]. Random testing results showed that on average, shear forces and normal forces can be predicted with a root mean square error (rms) of 0.5N and 1N, respectively. The average rms error in the measurement of shear forces is approximately 10% of the shear force range, making it useful for human-machine interaction. However, the large average rms error of the normal force is unsatisfactory and limits the utility of the sensors as the range of normal forces is only 0-3N. Therefore, to allow the sensor to be more useful, a more intelligent configuration of the LEDs and photodetectors is required as it is anticipated to improve the sensor's performance for the variables of interest.

An alternative approach for measuring fingertip touch forces, proposed by Sun, Hollerbach and Mascaro [11], uses an external camera system to image the fingernail and surrounding skin. Results indicated a complex pattern of coloration under applied force across the fingernail area and surrounding skin. Particularly, the middle region of the fingernail has a low force range (0-2N), the front region has an intermediate force range (2-6N), while the skin has a high force range (3-6N). By imaging the coloration changes in the fingernail and skin, normal and shear fingertip touch forces can be estimated with an accuracy of 5%-10% for a force range up to 10N. Further experiments have been

conducted to infer fingertip force direction during planar contact [12, 13], where fingernail images of 15 human subjects were registered to reference images and then warped to an atlas to extract common coloration features corresponding to force direction. This resulted in an overall force direction recognition accuracy of 94%.

In comparison to the results obtained using the original fingernail sensor, the fingernail imaging approach produced more accurate results and double the range of forces that can be measured. On the other hand, the use of an external camera system presents challenges of keeping the fingernail in view, and handling image registration, none of which is an issue with the original sensor. Given that, we propose redesigning the configuration of LEDs and photodetectors through the analysis of a photographic catalog composed of average fingernail coloration patterns of 15 human subjects. The resulting optoelectronic configuration is anticipated to optimize fingertip force direction estimation capabilities of the fingernail sensor.

Previously, an optical model that describes light transmittance between an LED and a photodiode in the fingernail area was introduced by Abu-Khalaf and Mascaro in [14] and improved to take into account the camera's sensitivity in [15]. In this paper, we use experimentally-determined light transmittance change through the nail bed, evaluated at the optimal wavelength, to calibrate the optical model using nonlinear least square parameter estimation. Subsequently, the calibrated model is used to predict the optimal optoelectronic configuration by incorporating experimentally-determined optimal separation distance between an LED/photodetector pair. The resulting optimal optoelectronic configuration is validated by examining its ability to classify the correct

force direction of test images of 6 different force poses for 15 human subjects, using a two- stage classifier.

A reduced configuration is derived from the optimal optoelectronic locations in order to facilitate the fabrication of the optimized fingernail sensor. Finally, the resulting classification accuracy is compared to force direction recognition accuracy obtained by imaging the coloration changes in the fingernail and surrounding skin, where a Bayesian classifier was implemented.

Background

In the original fingernail sensor, the optoelectronic devices were spatially arranged over the fingernail area in a laterally symmetric configuration, as shown in Figure 3.1(a). The LEDs were placed between the photodiodes to ensure that each photodiode has at least one neighboring LED. The role of each of the photodetectors was investigated in terms of the effect of removing one or more on force estimation. The analysis suggested designing the next generation of fingernail sensors with fewer photodetectors, as shown in Figure 3.1(b).

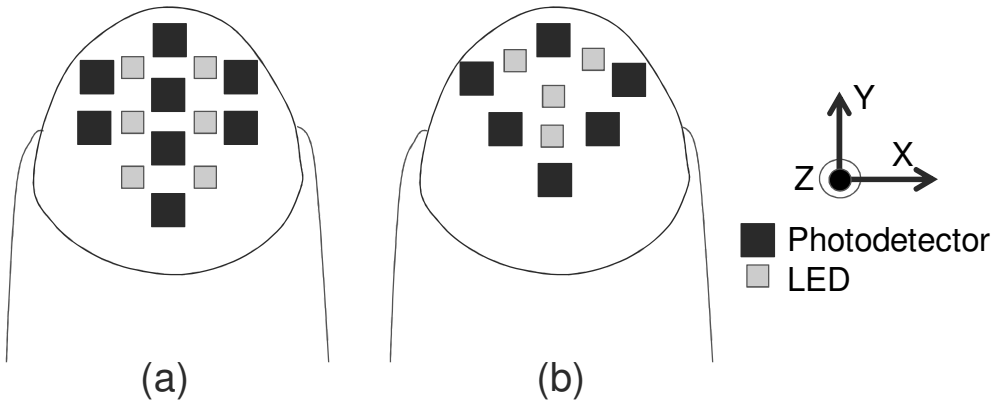

Figure 3.1 Spatial optoelectronic configuration. (a) Original fingernail sensor and (b) recommended configuration for next generation of fingernail sensors.

However, an optimal redesign cannot be simply achieved by removing one or more photodetectors while leaving the other optical components in their original configuration. Instead, the significance of the configuration of the optoelectronic devices, embedded in the fingernail sensor, needs to be investigated in terms of its affect on light transmittance through the fingernail.

The optical parameters for the transmittance of light through the human fingernail bed were evaluated by Abu-Khalaf and Mascaro in [14, 15]. Results indicated that the optimal parameters are located at a wavelength of 525nm and a path length of 2.5mm, which is the minimum separation distance between a LED/PD pair based on the size of our choice of optoelectronic devices. Hence, the new optoelectronic configuration has to incorporate the optimal separation distance in order to enhance the fingernail sensor force prediction capabilities.

Based on the high accuracy of force recognition obtained using the fingernail imaging approach, we propose redesigning the configuration of LEDs and photodetectors by analyzing the photographic catalog shown in Figure 3.2. This catalog represents average fingernail coloration patterns of 15 human subjects, whose index fingernails were photographed in 6 different force poses [9]. The first image is the nominal pose where no force is applied on the fingertip. In the second image, a normal force of -3N is applied. Next, lateral and longitudinal shear forces of 2N, applied in the positive and negative directions, are added. Images were normalized to the same size and the intensity value for each pixel was averaged across all 15 subjects to create the photographic catalog. The resulting average fingernail coloration patterns were found to be generally representative of the population and significantly distinct [9].

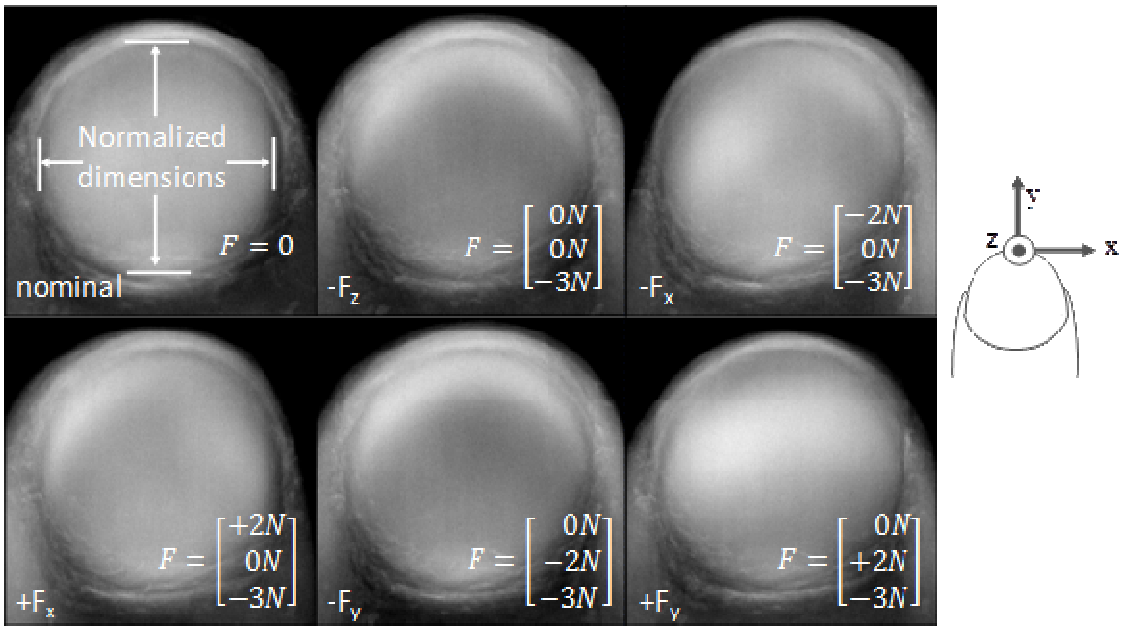

.

Figure 3.2 Average fingernail coloration patterns for 15 human subjects for 6 different force poses. Images were collected by S. Mascaro and H. Asada [9]. 5x contrast is applied for visual illustration.

The various force poses, shown in Figure 3.2, are defined with visible dark and white coloration zones corresponding to red (blood) and white (no blood) fingernail zones, respectively. Accordingly, for each pair of poses it is desired to locate two photodetector/LED pairs which distinguish between these coloration zones. This is achieved by constructing an optical model that describes light transmittance between an LED and a photodiode in the fingernail area, and subsequently predicts the optimal locations of the optoelectronic devices.

Optical Model

A CCD digital camera mounted above the fingernail, imaged fingernail coloration for 15 human subjects, while the fingertip is pressed against a force platform with various

forces. In order to compile the images into a photographic catalog, the size of each image was normalized according to the length and width of the fingernail. The resulting images are 400x400 pixels, with a 300x300 pixel fingernail in the center. Abu-Khalaf and Mascaro introduced an optical model [14], which describes light transmittance between an LED and a photodiode in the fingernail area based on intensity values of pixels in averaged fingernail images.

Figure 3.3 illustrates the conceptual optical model, where light transmitted between an optoelectronic pair is portrayed as a horizontal line passing through each of the pixels along its path. Each pixel has a width of δ_x, a depth of δ_y into the fingernail bed, and an absorption coefficient α. When the fingernail is imaged, light is transmitted from the camera into the nail with intensity I_{in} and after penetrating the nail bed light is reflected back to the camera with intensity I_{out}.

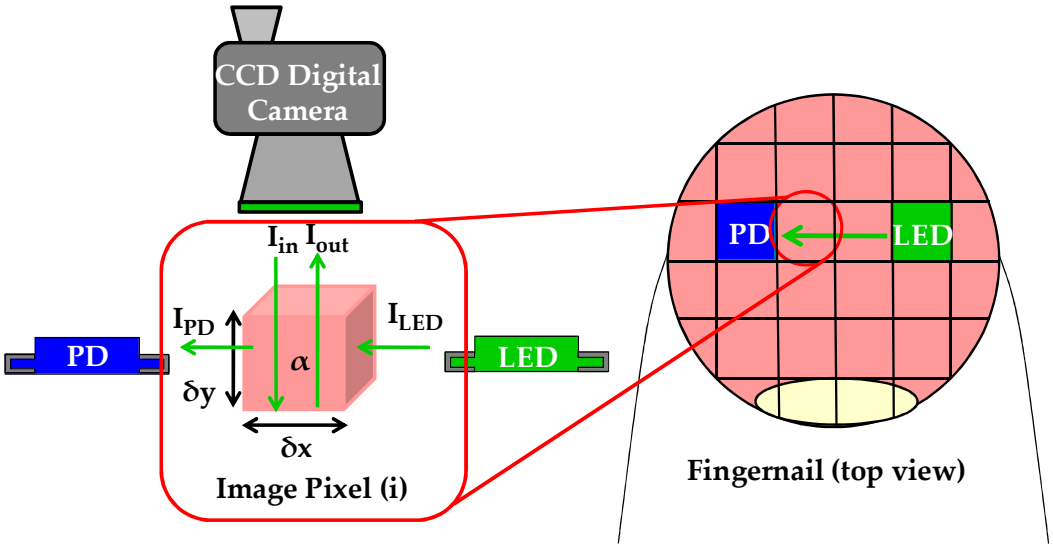

Figure 3.3 Optical model. Light transmittance between an LED and a photodiode in the fingernail area is shown as a horizontal line passing through each of the pixels along its path.

The absorption coefficient of the i^{th} pixel, α_i, can be evaluated using Beer-Lambert law, which states that there is a logarithmic dependence between the transmission of light through a medium and the product of the absorption coefficient of the medium, and the path length as follows

$$I_{out} = I_{in} \cdot e^{-2\alpha_i \delta_y} \tag{3.1}$$

Equation (3.1) is rearranged to express the absorption coefficient in terms of the transmitted and reflected light intensities, and the path length as follows

$$\alpha_i = -\frac{1}{2m\delta_x}\left[\ln\left(\frac{I_{out(i)}}{I_{in}}\right)\right] \tag{3.2}$$

where m is the ratio of the pixel depth to its width (δ_y / δ_x). For a path of n pixels light transmission can be expressed as

$$I_{PD} = I_{LED} \cdot e^{-\sum_{i=1}^{n} \alpha_i \delta_x} \tag{3.3}$$

where I_{PD} is the light intensity detected by the photodiode and I_{LED} is the intensity of light emitted by the LED. Substituting equation (3.2) in (3.3) results in

$$\frac{I_{PD}}{I_{LED}} = e^{\frac{1}{2m}[\ln(\mathrm{I_{out1}I_{out2}\cdots I_{outn}})]} \cdot e^{-\frac{n}{2m}[\ln(\mathrm{I_{in}})]} = \frac{[\mathrm{I_{out1}I_{out2}\cdots I_{outn}}]^{\frac{1}{2m}}}{[\mathrm{I_{in}}]^{\frac{n}{2m}}} \tag{3.4}$$

Based on equation (3.4), in order to locate LED/photodetector pairs which optimize force direction distinguishability between two force poses A and B, it is required to maximize the difference of the product of reflected light intensities along the path the light travels between an LED and a photodiode in each pose, as follows

$$MAX\left[\frac{(\mathrm{I_{out1A}I_{out2A}\cdots I_{outnA}})^{\frac{1}{2m}} - (\mathrm{I_{out1B}I_{out2B}\cdots I_{outnB}})^{\frac{1}{2m}}}{(\mathrm{I_{in}})^{\frac{n}{2m}}}\right] \tag{3.5}$$

The reflected light intensity of the i^{th} pixel, $I_{out(i)}$, falls in the range of 0-255 while the transmitted light intensity I_{in} is equal to 255 assuming perfect transmission from the camera to the surface of the nail. Hence, equation (3.5) can be expressed as

$$MAX\left[(I_{1A}I_{2A}\ldots I_{nA})^{1/2m} - (I_{1B}I_{2B}\ldots I_{nB})^{1/2m}\right] \tag{3.6}$$

where I_i is the light intensity of the i^{th} pixel in the range of 0-1. The product of the light intensities of the pixels along the path light travels between an optoelectronic pair can be described in terms of the irradiance E, which is directly proportional to the photodiode voltage in response to incident light intensity [16]. This implies that the maximum from equation (3.6) will result in optimized force direction distinguishability between any two poses in the photographic catalog.

To account for the camera's sensitivity, Abu-Khalaf and Mascaro improved their optical model in [15], by defining the following

$$P_i = \beta I_i \tag{3.7}$$

where β is a constant defined by the camera's sensitivity and P_i is the new image pixel intensity between 0 and 1. Substituting (3.7) in (3.6) results in

$$MAX\left[\left(\frac{P_{1A}P_{2A}\dots P_{nA}}{\beta^n}\right)^{1/2m} - \left(\frac{P_{1B}P_{2B}\dots P_{nB}}{\beta^n}\right)^{1/2m}\right] \tag{3.8}$$

Model Calibration

The path length n in equation (3.8) is defined as the number of pixels along the path light travels between an LED/photodiode pair. Previously, we located the optimal separation distance between an optoelectronic pair at 2.5mm. Based on the average dimensions of fingernails of 7 human subjects, the optimal separation distance translates into 60 pixels on a 300x300 pixel fingernail image. Hence, the maximum in equation (3.8) is evaluated at $n = 60$.

In addition to determining the optimal optical parameters, we also experimentally quantified the change in light transmittance through the fingernail bed ΔT_{FB} under varying force, which can be expressed as

$$\Delta T_{FB} = \left(\frac{P_{1A}P_{2A}\ldots P_{nA}}{\beta^n}\right)^{1/2m} - \left(\frac{P_{1B}P_{2B}\ldots P_{nB}}{\beta^n}\right)^{1/2m} \quad (3.9)$$

Hence, parameters m and β can be evaluated based on the experimentally-determined change in light transmittance through the fingernail bed. This is a nonlinear estimation problem which can be solved using a nonlinear least-squares approach [17].

Previously, ΔT_{FB} was characterized as a function of applied force, by instructing test participants to alternate between two force poses A and B. The nominal and $+F_y$ force poses, from the photographic catalog shown in Figure 3.2, were chosen as it is fairly natural to manually alternate between them. Since it is desired to optimize force direction distinguishability between the two force poses, the quantity ΔT_{FB} in equation (3.9) is experimentally determined at the optimal wavelength (525nm) and 3 different separation distances, as illustrated in Figure 3.4.

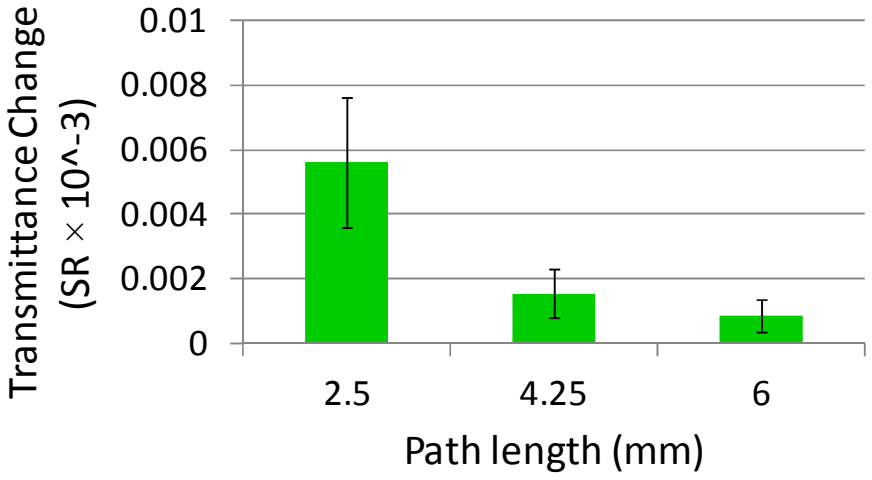

Figure 3.4 Average light transmittance change through the nail bed to a wavelength of 525nm and various path lengths. Data for 16 human subjects were averaged and plotted with error bars corresponding to the standard deviations.

During each experiment, a sensor was mounted on the fingernail such that an LED/photodiode pair is located where the fingernail coloration zones change notably between the two force poses. Similarly, to evaluate the product of image pixel intensities ($P_1P_2\ldots P_n$) along any of the examined path lengths, the optoelectronic pair is also located on each force pose image where the coloration zones vary between the poses. Figure 3.5 exemplifies the placement of an optoelectronic pair on the images of the two desired forces at the optimal separation distance.

Returning to equation (3.9), the change in light transmittance through the fingernail bed can be written in functional form as

$$y_c^i = \left(\frac{P_F}{b^n}\right)^a - \left(\frac{P_0}{b^n}\right)^a \qquad i = 1, \ldots, R \tag{3.10}$$

$$= f\left(P_F^i, P_0^i, \varphi\right) \tag{3.11}$$

$$= f^i(\varphi) \tag{3.12}$$

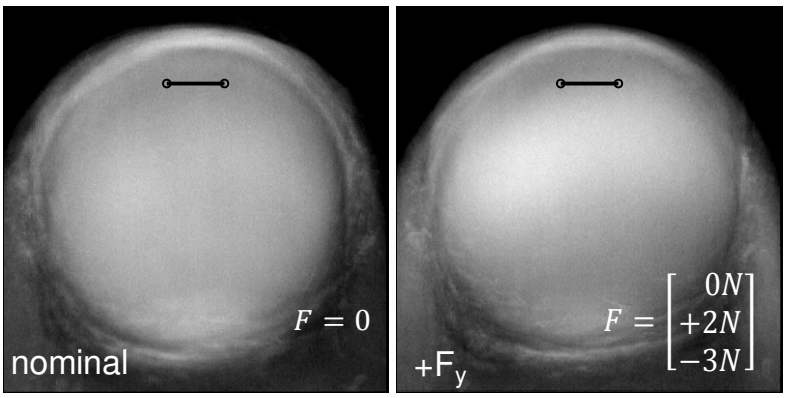

Figure 3.5 Applied force poses. Optoelectronic pair is placed where the coloration zone changes from red to white between nominal and $+F_y$ force poses, respectively.

where the light transmittance change y_c^i is a function of the input variables P_F and P_0 and parameters φ in equation (3.11). Since the product of image pixel intensities P at each pose can be considered as constant, the input variables are folded into the function in equation (3.12). The function is evaluated at R measurements which correspond to the various examined path lengths. The least squares sum to be minimized is

$$\min_{\varphi, y_c^i} S = \sum_{i=1}^{R} \left(e^i\right)^2 \equiv \sum_{i=1}^{R} \left(y^i - y_c^i\right)^2 \quad \text{subject to} \quad y_c^i = f^i(\varphi) \tag{3.13}$$

The solution of this nonlinear optimization problem is achieved by presenting it more generally [17]. Hence, we consider an arbitrary nonlinear vector function with error vector $\boldsymbol{e}^i$ which describes the measurement error in $\boldsymbol{y}^i$ as follows

$$\boldsymbol{y}^i \equiv \boldsymbol{f}^i(\varphi) + \boldsymbol{e}^i \tag{3.14}$$

where the input variables are folded into the function $\boldsymbol{f}^i$. Subject to $\boldsymbol{y}_c^i = \boldsymbol{f}^i(\varphi)$, the least square sum to be minimized, assuming output error only, is

$$\min_{\varphi, \boldsymbol{y}_c^i} S = \sum_{i=1}^{R} \left(\boldsymbol{e}^i\right)^T \boldsymbol{e}^i \equiv \sum_{i=1}^{R} \left(\boldsymbol{y}^i - \boldsymbol{y}_c^i\right)^T \left(\boldsymbol{y}^i - \boldsymbol{y}_c^i\right) \tag{3.15}$$

Equation (3.15) can be linearized using a Taylor series expansion performed around an estimate of the parameters φ^k at iteration k

$$\boldsymbol{y}_c^i \approx \boldsymbol{f}^i(\varphi^k) + \boldsymbol{C}^i \Delta\varphi \tag{3.16}$$

where $\boldsymbol{C}^i = \partial \boldsymbol{f}^i / \partial \varphi$ is the Jacobian evaluated at φ^k. By substituting equation (3.16) into (3.15), the minimization turns into an unconstrained problem as follows

$$\min_{\Delta\varphi} S \equiv \sum_{i=1}^{R} \left(\Delta \boldsymbol{y}^i - \boldsymbol{C}^i \Delta\varphi\right)^T \left(\Delta \boldsymbol{y}^i - \boldsymbol{C}^i \Delta\varphi\right) \tag{3.17}$$

where $\Delta \boldsymbol{y}^i = \boldsymbol{y}^i - \boldsymbol{f}^i(\varphi^k)$. For path lengths of 2.5mm, 4.25mm and 6mm equation (3.17) is expressed as

$$\min_{\Delta\varphi} S = (\Delta \boldsymbol{y} - \boldsymbol{C}\Delta\varphi)^T (\Delta \boldsymbol{y} - \boldsymbol{C}\Delta\varphi) \quad \text{where } \boldsymbol{C} = \begin{bmatrix} \boldsymbol{C}^1 \\ \boldsymbol{C}^2 \\ \boldsymbol{C}^3 \end{bmatrix}, \Delta \boldsymbol{y} = \begin{bmatrix} \boldsymbol{y}^1 \\ \boldsymbol{y}^2 \\ \boldsymbol{y}^3 \end{bmatrix} \tag{3.18}$$

Using ordinary least squares, the minimization can be solved as

$$\Delta\varphi = (\boldsymbol{C}^T \boldsymbol{C})^{-1} \boldsymbol{C}^T \Delta \boldsymbol{y} \tag{3.19}$$

This linearization procedure assumes that our current estimate φ^k is close to the correct solution. Hence, by adding a small correction factor $\Delta\varphi$ we get a new parameter estimate

$$\varphi^{k+1} = \varphi^{k} + \Delta\varphi \tag{3.20}$$

Using the Gauss-Newton method, we start with an initial estimate φ^{0} of the parameters a and b in equation (3.10) as our first iteration and continue iterating until $\Delta\varphi$ is smaller than an appropriate constant ε. Returning to our model, for path length n = [60, 102, 144] ^{T} in pixels, equation (3.10) can be stacked into vectors as follows

$$\begin{aligned} \mathbf{y} &= \left(\frac{\boldsymbol{P}_F}{b^n}\right)^a - \left(\frac{\boldsymbol{P}_0}{b^n}\right)^a + \boldsymbol{e} \\ &\equiv \boldsymbol{f}(\varphi) + \boldsymbol{e} \end{aligned} \tag{3.21}$$

where

$$\boldsymbol{y} = \begin{bmatrix} y^1 \\ y^2 \\ y^3 \end{bmatrix}, \qquad \boldsymbol{P_F} = \begin{bmatrix} {P_F}^1 \\ {P_F}^2 \\ {P_F}^3 \end{bmatrix}, \qquad \boldsymbol{P_0} = \begin{bmatrix} {P_0}^1 \\ {P_0}^2 \\ {P_0}^3 \end{bmatrix}, \qquad \boldsymbol{f} = \begin{bmatrix} f^1 \\ f^2 \\ f^3 \end{bmatrix}, \qquad \boldsymbol{e} = \begin{bmatrix} e^1 \\ e^2 \\ e^3 \end{bmatrix}$$

The vector $\boldsymbol{y}$ corresponds to the light transmittance change plotted in Figure 3.4. P_F and P_0 are the products of image pixel intensities measured along the path length n at the $+F_y$ and nominal force poses, respectively. The Jacobian $\boldsymbol{C}$ is found by differentiating equation (3.13) to parameters a and b. The results of implementing this nonlinear least squares approach in Matlab are plotted in Figure 3.6. We began the estimation with a = 1/90 and b = 0.9. The estimation results in m = 1/2a = 18.95 and $\beta = b$ = 1.7121.

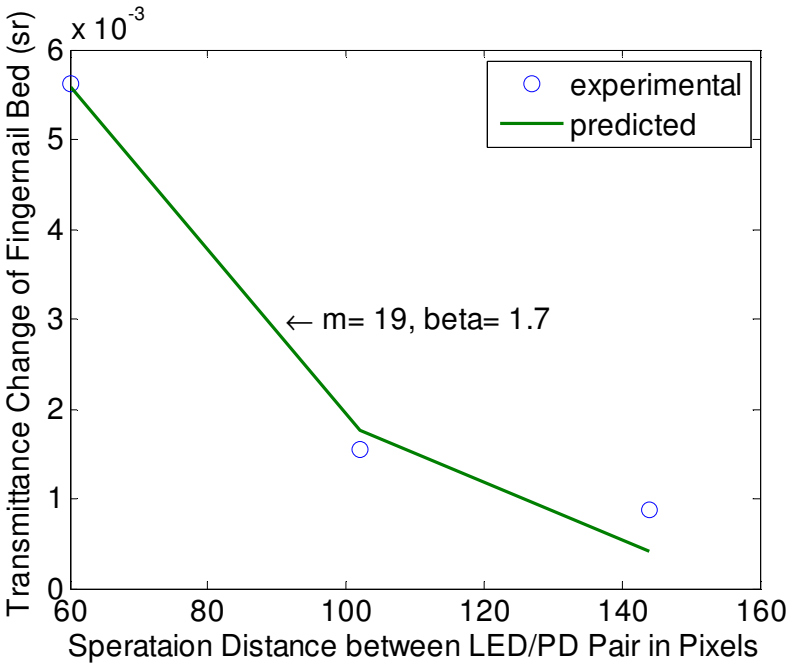

Figure 3.6 Parameter estimation results. Data obtained from fingernail images (solid line) are fitted to experimental data of light transmittance change ('o').

Optoelectronic Configuration

Subsequent to model parameter estimation, to determine locations of LED/photodetector pairs which optimize force direction distinguishability, each two force poses in the photographic catalog (A and B) can be compared using the following equation

$$\frac{(P_{1A}P_{2A}\dots P_{nA})^{0.026} - (P_{1B}P_{2B}\dots P_{nB})^{0.026}}{2.31} \tag{3.22}$$

To minimize the computation time needed to locate the optimal optoelectronic pairs, each fingernail image was divided into a 50x50 pixel grid. The intensity of each new pixel is set to the mean of the pixels intensities in each 6x6 block of the input image.

The fingernail images are cropped to 300x300 pixel images to only include the normalized area of the fingernail, shown in the photographic catalog. The nail lunula which is the visible part of the root of the nail and appears as a crescent-shaped whitish area in the fingernail images, is removed as it is not useful for force direction estimation. The white area shown in Figure 3.7 represents the fingernail area where the optimal optoelectronic configuration will be located.

For each two force poses in the photographic catalog, the search algorithm defines a set of "seed" points corresponding to the coordinates of the center of each 6x6 block of the input image within the useful fingernail area. On each image, the 8 neighboring pixels of the seed point, located at the optimal separation distance of 60 pixels, are inspected. The algorithm applies equation (3.22) to find the difference of the product of pixel intensities along the path between the seed point and each of its neighbors in each pose. Once all neighbors are inspected, the seed point is labeled to avoid evaluating the same pair of points twice. This procedure is repeated until all seed points are labeled.

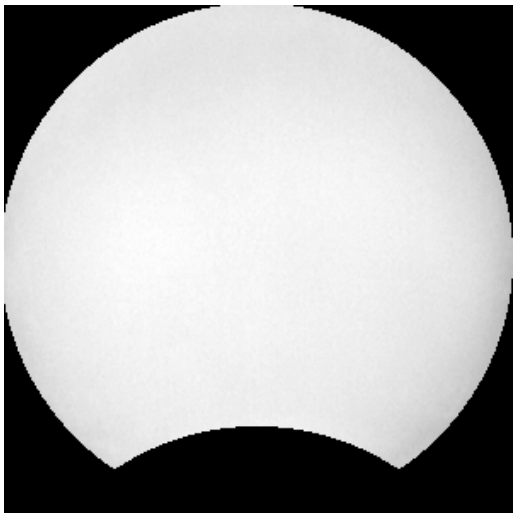

Figure 3.7 Useful fingernail area. The white area represents the subset used for locating the optoelectronic configuration.

The algorithm returns the coordinates of the optoelectronic pairs which produce the maximum positive and negative differences of the product of pixel intensities in equation (3.22). For example, when comparing the negative and positive lateral shear force poses ($-F_x$ and $+F_x$), the algorithm locates two optimal optoelectronic pairs, as shown in Figure 3.8 (a) and (b), where light travels between an optimal emitter/detector pair with interchangeable locations. While the algorithm searched images with natural contrast, 5x contrast was applied to the images in Figure 3.8 to illustrate that the optoelectronic pairs are in fact located where the fingernail coloration noticeably varies between the two force poses.

The algorithm was applied to the rest of the force poses in the photographic catalog, where two optimal optoelectronic pairs were located for each two force poses, resulting in 30 optimal optoelectronic pairs demonstrated in Figure 3.9. Each pair is connected by a line representing the light path between an emitter ('o') and a detector ('*') of interchangeable locations.

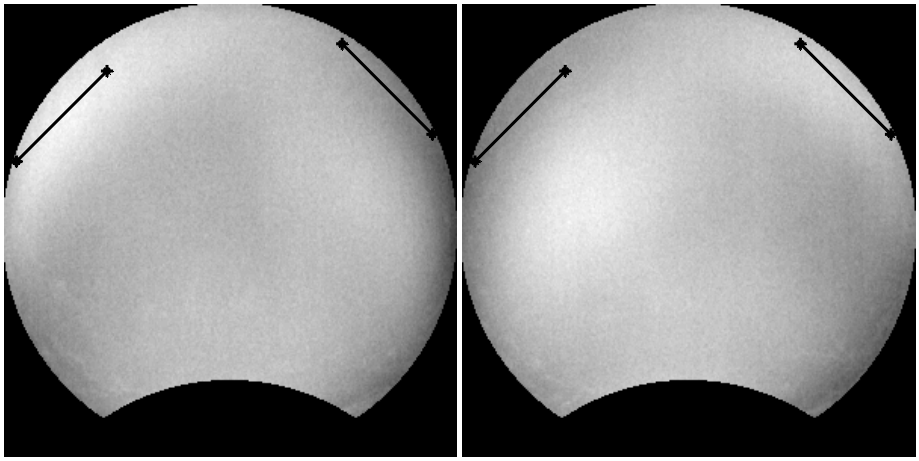

Figure 3.8 Optimal optoelectronic pairs when comparing (a) negative lateral shear force pose $-F_x$ and (b) positive lateral shear force pose $+F_x$. 5x contrast applied.

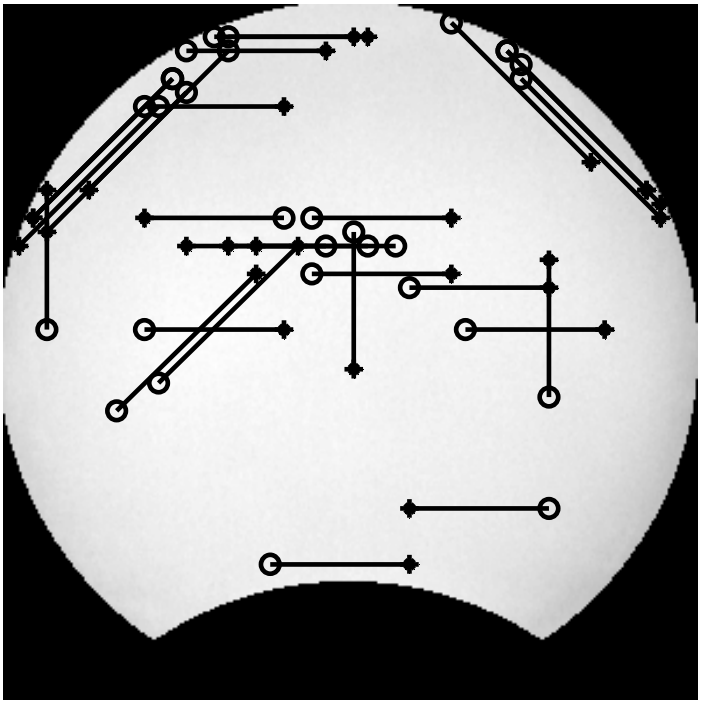

Figure 3.9 Optimal optoelectronic configuration. There are 28 unique optoelectronic pairs with emitters (‘o’) and detectors (‘*’) of interchangeable locations.

The normal force $-F_z$ and negative longitudinal shear force $-F_y$ do not result in a statistically significant difference in coloration [9]. Therefore equation (3.22) only results in a positive maximum at which the optimal optoelectronic pair for this pose pair is located. The other optoelectronic pair is chosen to produce the second highest positive difference of the product of pixel intensities.

The resulting optimal configuration suggests that we can use fewer emitters and detectors by replacing adjacent components with one emitter or detector, provided that the sensor’s performance is not jeopardized. This is supported by the fact that LEDs and photodetectors, though miniature, are of a significant size relative to image pixels. Hence, the proposed optimal configuration is subject to further analysis and testing.

Classification

Consequently, the performance of the optimal optoelectronic configuration is evaluated by examining its ability to classify the correct force direction of test images of 15 human subjects. For each human subject 10 images were collected at each of the force poses of interest; F_{zero} (nominal), $-F_z$, $-F_x$, $+F_x$, $-F_y$, and $+F_y$. Since we are only interested in predicting force direction, the images were collected at various force magnitudes. Out of the 10 images, 5 are used as training images and the remaining 5 are used for validation.

Linear Discriminant Multicategory Classifier

As demonstrated in the previous section, each two force poses can be distinguished by two optoelectronic pairs (pose pair), and so for the 15 different force pose combinations we have 15 pose pairs (or 30 optimal optoelectronic pairs). Consequently, for any given force pose i, we define the component ΔV as the difference between the output voltages from each pose pair as follows

$$\Delta V_{jk} = V_{a\,jk} - V_{b\,jk} \qquad j,k = 1,\dots,6 \quad j \neq k \tag{3.23}$$

In practice, ΔV is the difference between the outputs of the two photodetectors (a and b) in each pose pair. For a test image, ΔV can be expressed as

$$\Delta V = \left(\frac{P_{1a}P_{2a}\dots P_{na}}{\beta^n}\right)^{1/2m} - \left(\frac{P_{1b}P_{2b}\dots P_{nb}}{\beta^n}\right)^{1/2m} \tag{3.24}$$

where P_i is the image pixel intensity between 0 and 1, n is the path length between an emitter/detector pair, and m and β are the parameters previously estimated from the optical model calibration.

The simplest model that can be used to construct a force direction classifier is a linear model. Hence, we define our classifier as a discriminant function [18] that is a linear combination of the components of $\boldsymbol{\Delta V}$ as follows

$$g_i(\Delta \boldsymbol{V}) = \boldsymbol{w_i^T}\Delta \boldsymbol{V} + w_{i0} \qquad i = 1, \ldots, 6 \tag{3.25}$$

where $\boldsymbol{w}$ is the weight vector and w_0 is the bias. $\boldsymbol{\Delta V}$ is an mx1 vector of output voltage differences and can be redefined as

$$\Delta \boldsymbol{V} = \begin{bmatrix} 1 \\ \Delta V_{12} \\ \Delta V_{13} \\ \vdots \\ \Delta V_{\mathrm{jk}} \end{bmatrix} = \begin{bmatrix} 1 \\ \Delta V_1 \\ \Delta V_2 \\ \vdots \\ \Delta V_{\mathrm{m}} \end{bmatrix} \tag{3.26}$$

Accordingly, the multicategory classifier becomes

$$g_i(\Delta \boldsymbol{V}) = \boldsymbol{w_i^T}\Delta \boldsymbol{V} \qquad \text{where } \boldsymbol{w_i^T} = \begin{bmatrix} w_{i0} \\ w_{i1} \\ \vdots \\ w_{i\mathrm{m}} \end{bmatrix} \tag{3.27}$$

where m is the number of output voltage differences. For n training images, the classifier equation can be rewritten using matrix notation, as follows

$$\mathbf{B} = \mathbf{W^T}\Delta\mathbf{V} \tag{3.28}$$

$$= \begin{bmatrix} w_{10} & \cdots & w_{1\mathrm{m}} \\ w_{20} & \cdots & w_{2\mathrm{m}} \\ \vdots & \vdots & \vdots \\ w_{60} & \cdots & w_{6\mathrm{m}} \end{bmatrix} \begin{bmatrix} 1 & 1 & \cdots & 1 \\ \Delta V_{11} & \Delta V_{12} & \cdots & \Delta V_{1\mathrm{n}} \\ \vdots & \vdots & \vdots & \vdots \\ \Delta V_{\mathrm{m}1} & \Delta V_{\mathrm{m}2} & \cdots & \Delta V_{\mathrm{mn}} \end{bmatrix}$$

where B is a 6xn matrix of training data with each row corresponding to one of the 6 force poses. For each training image, the row corresponding to the correct force pose is labeled 1 while all other rows are labeled -1. To find the weight matrix **W**, one approach is to implement least squares regression using the pseudoinverse [18] as follows

$$\mathbf{W} = \mathbf{B}\Delta\mathbf{V^T}(\Delta\mathbf{V}\Delta\mathbf{V^T})^{-1} \tag{3.29}$$

To improve the conditioning of the inverse problem, Tikhonov regularization (ridge regression) is implemented

$$\mathbf{W} = \mathbf{B}\Delta\mathbf{V^T}(\Delta\mathbf{V}\Delta\mathbf{V^T} + \mathbf{\Gamma\Gamma^T})^{-1} \tag{3.30}$$

where $\Gamma = \alpha I$, α is the Tikhonov factor, and I is the identity matrix. The optimal parameter α is found iteratively to be equal to 0.001.

After determining the weight matrix **W**, equation (3.27) can be used to predict the force direction for a new set of test images. For each test image, the vector $\boldsymbol{\Delta V}$ is computed and subsequently the 6x1 array g is evaluated. The 6 different rows in g

correspond to the 6 force poses of interest. The rows are compared and the image is assigned the class of the row with the largest value.

Distinction of $-F_z$ and $-F_y$

As stated earlier, the force poses $-F_z$ and $-F_y$ do not result in a statistically significant difference in coloration, and accordingly are not clearly separable. Hence, we modify our classifier to allow for enhanced force direction distinguishability. This is simply achieved by breaking up the classification process into two stages, as illustrated in Figure 3.10. In the first stage, the linear multicategory classifier introduced earlier is used to distinguish between each two force poses in the photographic catalog except for the unlikely separable pair $-F_z$ and $-F_y$. Namely, the output voltage difference from the pose pair, which is responsible for distinguishing between $-F_z$ and $-F_y$, is not included in the vector $\boldsymbol{\Delta V}$. Subsequently, the training is carried out to determine the weight matrix $\mathbf{W}$, and a test image is classified based on equation (3.27).

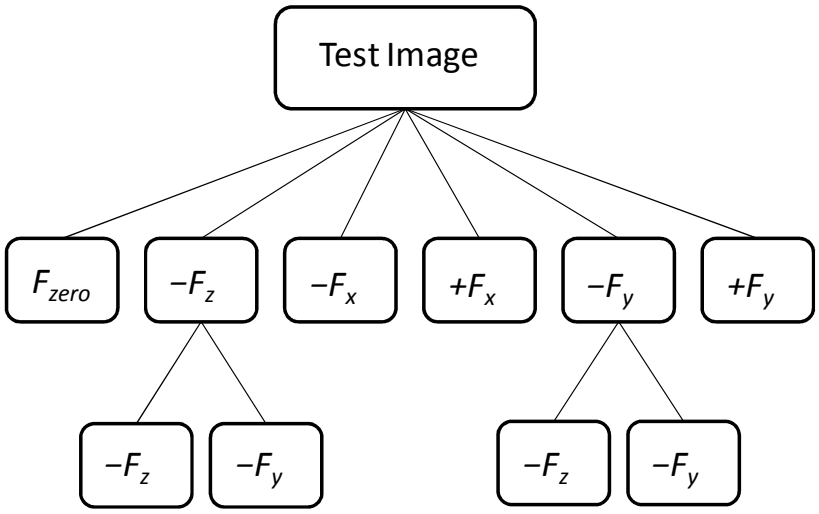

Figure 3.10 Classification process. In the first stage, a linear multicategory classifier is implemented, while in the second stage $-F_z$ and $-F_y$ are distinguished using a pairwise classifier.

The classification process ends if a test image is classified as F_{zero}, $-F_x$, $+F_x$, or $+F_y$. Otherwise, if the image is classified as $-F_z$ or $-F_y$, the classification moves to the second stage, where a pairwise classifier is implemented. One could think of the second stage as a reclassification of the force poses in question, where the previously excluded pair pose is used to distinctively classify the test image.

The output voltage difference ΔV from the pose pair of interest is evaluated for each training image and the results are averaged for each force pose to determine the threshold T_{zy}, as follows

$$T_{zy} = \frac{\Delta\bar{V}_z + \Delta\bar{V}_y}{2} \tag{3.31}$$

where $\Delta\bar{V}_z$ and $\Delta\bar{V}_y$ are the average pose pair outputs from the force poses $-F_z$ and $-F_y$, respectively. The linear decision boundary T_{zy} separates the averaged training data such that a test image is inspected as illustrated in the following algorithm

if $\Delta\bar{V}_z > \Delta\bar{V}_y$

if $\Delta V_{TEST} > T_{zy}$, class $= -F_z$

else if $\Delta V_{TEST} < T_z$, class $= -F_y$

else if $\Delta\bar{V}_z < \Delta\bar{V}_y$

if $\Delta V_{TEST} < T_{zy}$, class $= -F_z$

else if $\Delta V_{TEST} > T_{zy}$, class $= -F_y$

end

Results

The two-stage classifier was individually trained for each of the 15 test participants in order for the training data to be linearly separable. The classification results for the 15 human subjects for 450 test images of the 6 force poses are demonstrated in Table 3.1. The overall accuracy is 93%, where 10 out of the 15 human subjects have an accuracy of at least 90%. Four human subjects have an accuracy of 100%, while the lowest accuracy is 83%.

Table 3.1 Classification results for 15 test participants. The overall accuracy is 93 %.

Subject	**Classification Accuracy%**
1	100
2	100
3	97
4	93
5	87
6	93
7	87
8	100
9	97
10	87
11	83
12	90
13	93
14	100
15	87
Average	**93**

In Table 3.2, the accuracy for all human subjects for each force direction is shown, where all force poses except for one have accuracies above 90% and the lowest accuracy of 87% is located at $+Fy$.

Discussion

Evidently, the classification results validate the proposed optimal optoelectronic configuration as well as the optical model leading to it. However, to get the most accurate optimal locations of the optoelectronic devices, they are assumed of the size of a 6x6 pixel block. In reality, though the devices are miniature, they are of a significant size when compared to an image pixel. Moreover, the fabrication of the optimized fingernail sensor is rather intricate with 60 LEDs and photodetectors. Hence, a reduced configuration is derived from the optimal one; in order to facilitate the fabrication of the optimized fingernail sensor without significantly compromising the classification accuracy.

Table 3.2 Classification results for each of the 6 force poses of interest.

Force Pose	**Classification Accuracy%**
F_{zero}	95
$-F_z$	95
$-F_x$	95
$+F_x$	93
$-F_y$	93
$+F_y$	87
Average	**93**

Modified Configuration

Based on the average dimensions of fingernails of 7 human subjects, the effective light detecting area of our choice of photodiode translates into a 20x20 pixel block on a 300x300 pixel fingernail image. The area of our choice of LED translates into a 30x30 pixel block, thus for consistency we standardize the size of an optoelectronic device to a 20x20 pixel block. To incorporate the size of the optoelectronic devices into the optimal configuration, the devices are kept at their optimal locations while the optimal path is inspected on a 15x15 pixel grid. The intensity of each new pixel is set to the mean of the pixels intensities in each 20x20 pixel block of the input image.

The optimal configuration, shown in Figure 3.11(a), suggests that fewer emitters and detectors can replace adjacent components, provided that the sensor's performance is not jeopardized. The reduced configuration is shown in Figure 3.11(b), where 5 LEDs and 4 larger photodiodes replace the 60 optimal optoelectronic devices.

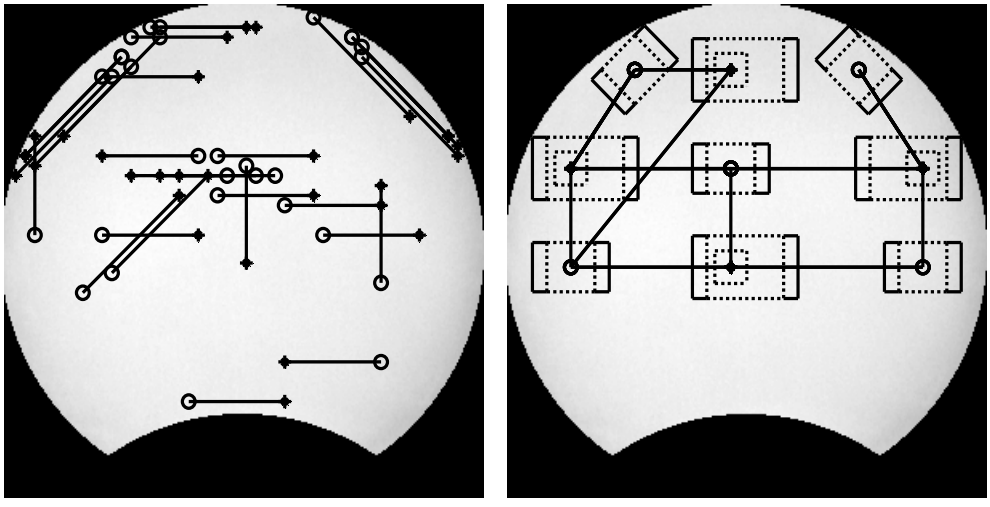

Figure 3.11 Optimal and reduced optoelectronic configurations. (a) The optimal configuration locates 60 optoelectronic devices on the fingernail, while (b) the reduced configuration only includes 5 LEDs and 4 larger photodiodes.

The actual size of the LEDs and photodetectors is added to the reduced configuration to demonstrate the feasibility of designing a fingernail sensor with this configuration. The optoelectronic devices in the reduced configuration were mainly located where the optimal components are clustered. Other scattered components were moved to the nearest cluster of optoelectronics. The optoelectronic pairs in Figure 3.11 are connected with a line representing the light path between an emitter ('o') and a detector ('*').

Concisely, the proposed optimal configuration was first modified by incorporating the size of the optoelectronic devices. Next, the number of optoelectronic devices was reduced to facilitate the fabrication of the fingernail sensor. The effect of these changes on the classification accuracy is examined for the 15 human subjects for 450 test images of the 6 force poses as demonstrated in Table 3.3. Including the actual size of the optoelectronic devices improved the overall accuracy from 93% to 97%.

The reduced configuration was also tested on a 15x15 grid to include the actual size of the optoelectronic devices, resulting in an overall accuracy of 95%. Twelve out of the 15 human subjects have an accuracy of at least 90%. Five human subjects have an accuracy of 100%, while the lowest accuracy is 83%. The improvement in the accuracy of the modified and reduced configurations is expected as the optimal locations are based on average images which may be slightly different for the individual images. Therefore, including the actual size of the optoelectronics covers a larger area on the test image and results in better classification.

Table 3.3 Classification results for 15 test participants for optimal, modified, and reduced configurations.

Subject	**Optimal Configuration Accuracy% (50x50 grid)**	**Modified Configuration Accuracy% (15x15 grid)**	**Reduced Configuration Accuracy% (15x15 grid)**
1	100	100	83
2	100	100	100
3	97	93	100
4	93	97	97
5	87	97	93
6	93	87	83
7	87	100	97
8	100	100	87
9	97	97	100
10	87	97	93
11	83	97	100
12	90	100	97
13	93	97	97
14	100	100	100
15	87	100	93
Average	**93**	**97**	**95**

In Table 3.4, the classification accuracy for all subjects for each force direction is shown for optimal, modified, and reduced configurations. Again as the actual size of optoelectronics is included, we see an improvement in the accuracy. Using the reduced configuration, all force poses except for one have accuracies of at least 96%, where the lowest accuracy of 80% is located at $+F_y$. The improved classification accuracy of the reduced configuration, though lower than that of the modified configuration, validates the use of fewer emitters and detectors.

Table 3.4 Classification results for each of the 6 force poses of interest for optimal, modified, and reduced configurations.

Pose	**Optimal Configuration Accuracy% (50x50 grid)**	**Modified Configuration Accuracy% (15x15 grid)**	**Reduced Configuration Accuracy% (15x15 grid)**
F_{zero}	95	99	97
$-F_z$	95	97	99
$-F_x$	95	100	97
$+F_x$	93	100	99
$-F_y$	93	95	96
$+F_y$	87	93	80
Average	**93**	**97**	**95**

An alternative approach for estimating fingertip force direction, proposed by Sun, Hollerbach and Mascaro [13], uses an external camera system to image the fingernail and surrounding skin during planar contact. Fingernail images of 15 human subjects were registered to reference images and then warped to an atlas to extract common coloration features corresponding to force direction. Without individual calibration, this approach resulted in an overall force direction recognition accuracy of 90%. The force directions $-F_z$ and $-F_y$ were found not separable for 40% of the test images and subsequently individual training was implemented to result in an overall force direction recognition accuracy of 94%.

The fingernail sensor can be viewed as a low resolution camera with limited detection at the proposed locations of the optoelectronic devices. Nevertheless, by using a more intelligent optoelectronic configuration based on optimized locations of LEDs and photodetectors we were able to achieve force direction recognition accuracy of 95%,

which is comparable to accuracy obtained using a high resolution external camera system.

The reduced configuration is also comparable to the optoelectronic configuration of the original fingernail sensor, as shown in Figure 3.12. The reduced configuration is more intelligent as it uses a smaller number of electronics to cover a wider area of the fingernail. Each 2 photodiodes in the original configuration in 3.12(a) are replaced by one photodiode in the reduced configuration in 3.12(b). Also the 2 LEDs in the center of the original configuration in 3.12(a) are replaced with one LED in 3.12(b).

Conclusion

In conclusion, this paper presented an optimal redesign of the optoelectronic configuration of the fingernail sensor, by introducing an optical model which describes

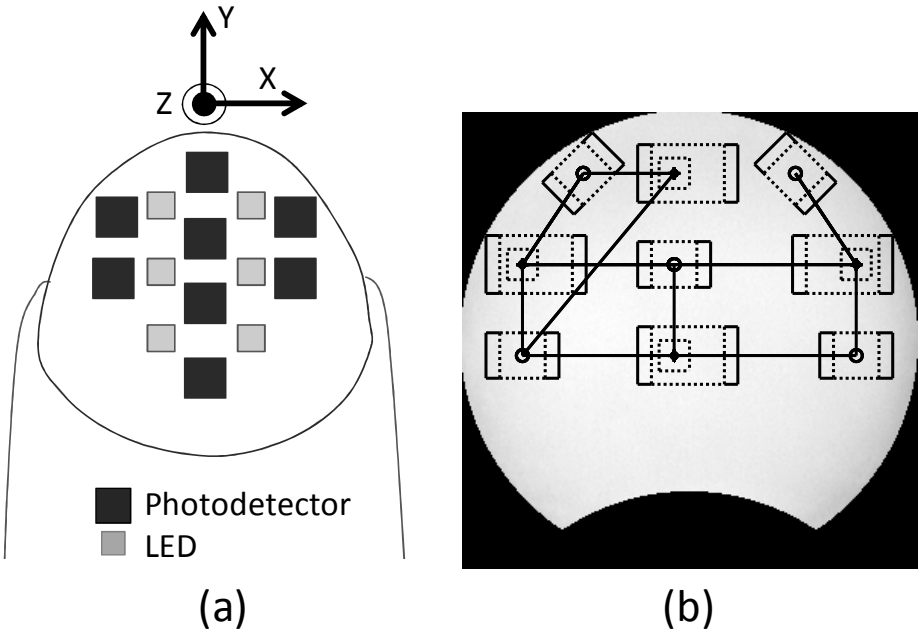

Figure 3.12 Original and reduced optoelectronic configurations. (a) Spatial configuration of original fingernail sensor and (b) proposed reduced optoelectronic configuration are comparable.

light transmittance between an LED and a photodiode in the fingernail area. The model was calibrated using experimentally-determined change in light transmittance through the fingernail bed at the optimal wavelength. A nonlinear least-squares approach was implemented to estimate the model's parameters.

The calibrated optical model was used to locate 30 optimal optoelectronic pairs on the useful fingernail area based on average fingernail coloration in order to optimize force direction distinguishability between the variables of interest. The resulting optimal optoelectronic configuration was validated by examining its ability to classify the correct force direction of test images. This was achieved by implementing a two-stage classifier; in the first stage a linear discriminant multicategory classifier was applied to all force poses. The normal and positive longitudinal shear force poses were reclassified in the second stage using a pairwise classifier. With individual training, the overall classification accuracy was 93% for 15 human subjects for 6 different force poses.

The optimal configuration was modified to incorporate the actual size of the optoelectronic components, resulting in a classification accuracy of 97%. Also a reduced configuration was derived from the optimal optoelectronic locations; in order to facilitate the fabrication of the optimized fingernail sensor without significantly compromising the classification accuracy. The proposed reduced configuration resulted in an overall recognition accuracy of 95%, which is comparable to that obtained using an external camera system.

In future work, we propose designing the next generation of fingernail sensors by embedding the reduced optoelectronic configuration in a stretchable platform to eliminate the need for customized fabrication for each individual user. The development of a new

stretchable sensor presents an intellectually rich set of challenges which requires using novel fabrication techniques to create a fully functional stretchable circuit containing embedded optoelectronic components. The performance of the novel sensor will be investigated in terms of its capability to predict force direction with high accuracy. With individual calibration, the classification procedure introduced in this paper can be applied to estimate fingertip force direction from experimental photodetector readings to experimentally validate the proposed optoelectronic configuration.

References

[1] J.G. Webster, Ed., Tactile Sensors for Robotics and Medicine. New York: Wiley, 1988.

[2] S. Mascaro and H. Asada, "Virtual switch human-machine interface using fingernail touch sensors," *Proc. IEEE Int. Conf. Robotics and Automation*, vol. 4, pp. 2533-2538, 1999.

[3] S. Mascaro and H. Asada, "Hand-in-glove human-machine interface and interactive control: Task process modeling using Petri Nets," *Proc. IEEE Int. Conf. Robot. Automat.*, vol. 2, pp. 1289–1295, 1998.

[4] H. Yun, D. Cannon, A. Freivalds, and G. Thomas, "An instrumented glove for grasp specification in virtual-reality-based point-and-direct telerobotics," *IEEE Trans. Syst. Man, Cybern. B*, vol. 27, pp. 835–846, 1997.

[5] S. Sato, M. Shimojo, Y. Seki, A. Takahashi, and S. Shimuzu, "Measuring system for grasping," *Proc. IEEE Int. Workshop Robot Human Commun.*, pp. 292–297, 1996.

[6] I. Kim and H. Inooka, "Determination of grasp forces for robot hands based on human capabilities," *Contr. Eng. Practice*, vol. 2, no. 3, pp. 415–420, 1994.

[7] D.J. Sturman and D. Zelzer, "A survey of glove-based input," *IEEE Computer Graphics & Applications*, pp. 30-39, January, 1994.

[8] S. Mascaro and H. Asada, "Photoplethysmograph fingernail sensors for measuring finger forces without haptic obstruction," *IEEE Trans. on Robotics and Automation*, vol. 17, no. 5, pp. 698–708, 2001.

[9] S. Mascaro and H. Asada, "The common patterns of blood perfusion in the fingernail bed subject to fingertip touch force and finger posture," *Haptics-e: The Electronic Journal of Haptics Research*, vol. 4, no. 3, pp. 1-6, 2006.

[10] S. Mascaro and H. Asada, "Measurement of finger posture and three-axis fingertip touch force using fingernail sensors," *IEEE Trans. on Robotics and Automation*, vol. 20, no. 1, pp. 26-35, 2004.

[11] Y. Sun, J. Hollerbach, and S. Mascaro, "Predicting fingertip forces by imaging coloration changes in the fingernail and surrounding skin, " *IEEE Transactions on Biomedical Engineering*, vol. 55, no. 10, pp. 2363-2371, 2008.

[12] Y. Sun, J. Hollerbach, and S. Mascaro, "Imaging the finger force direction," *IEEE Computer Society Conference on Computer Vision and Pattern Recognition (CVPR)*, pp. 1-6, June 18-23, 2007.

[13] Y. Sun, J. Hollerbach, and S. Mascaro, "Estimation of finger force direction with computer vision," *IEEE Transactions on Robotics*, vol. 25, no. 6, pp. 1356-1369, 2009.

[14] J. Abu-Khalaf and S. Mascaro, "Optimization of fingernail sensor design based on fingernail imaging," *Proceedings of the SPIE Novel Optical Systems Design and Optimization XIII*, vol. 7787, 8 pages, 2010.

[15] J. Abu-Khalaf and S. Mascaro, "Optimization of fingernail sensing technique based on optical experimentation and modeling," *Proceedings of the IEEE Sensors Applications Symposium (SAS)*, pp. 283-288, 2011.

[16] F. L. Pedrotti and L. S. Pedrotti, Introduction to Optics. Englewood Cliffs, NJ: Prentice-Hall, Inc., 1987.

[17] J. Hollerbach. Class Lecture. Class Lecture. System Identification for Robotics. University of Utah, Salt Lake City, UT. Spring, 2010.

[18] R. O. Duda, P. E. Hart, and D. G. Stork, Pattern Classification. New York: Wiley, 2001.

CHAPTER 4

OPTIMIZATION OF STRETCHABLE FINGERNAIL SENSOR FABRICATION BASED ON FINITE ELEMENT MODELING

Abstract

This paper describes the fabrication of a novel stretchable fingernail sensor, mounted on the fingernail to estimate fingertip force direction. The fingernail sensor is an optical reflectance photoplethysmograph sensor used to measure the change in blood perfusion in the nail bed, as the finger pad touches a surface with various forces. The original fingernail sensor was rigidly attached to the human fingernail and accordingly needed to be customized to the geometry of the fingernail. Namely, transparent epoxy was used to mold the sensor to a positive cast of the user's fingertip. Hence, to eliminate the need for customized fabrication for each individual user, it is desired to fabricate a stretchable fingernail sensor which is independent of the fingertip geometry. Though flexible printed circuits are commonplace, they can only bend in one dimension at a time. However, the human fingernail curvature is two-dimensional, necessitating a stretchable fingernail sensor to fully conform to the surface. In this paper, we develop novel fabrication techniques which overcome the challenges of patterning conductive lines on a stretchable substrate, and embedding rigid optical components in a stretchable platform

while maintaining electrical conductivity. When the sensor is loaded onto the fingernail surface, the reliability of the electrical connections is expected to be assisted by the concave bending of the substrate. Accordingly, a finite element analysis is conducted to optimize the electrical contact resistance as a function of the bending curvature and substrate thickness. In this paper, we demonstrate the successful fabrication of a prototype stretchable sensor with an embedded LED/photodetector pair, and test its functionality in relation to the design parameters.

Introduction and Background

Fingernail sensors have been developed for detecting fingertip touch force and finger posture based on the reflectance photoplythysmography technique [1], illustrated in Figure 4.1(a). A photodiode and LED pair is used to measure variations in capillary blood volume as a function of applied force. The LED illuminates the fingernail area while a nearby photodiode detects the reflected light intensity and produces a current proportional to it. Using the plethysmograph circuitry, shown in Figure 4.1(b), an output voltage varying with applied force is generated.

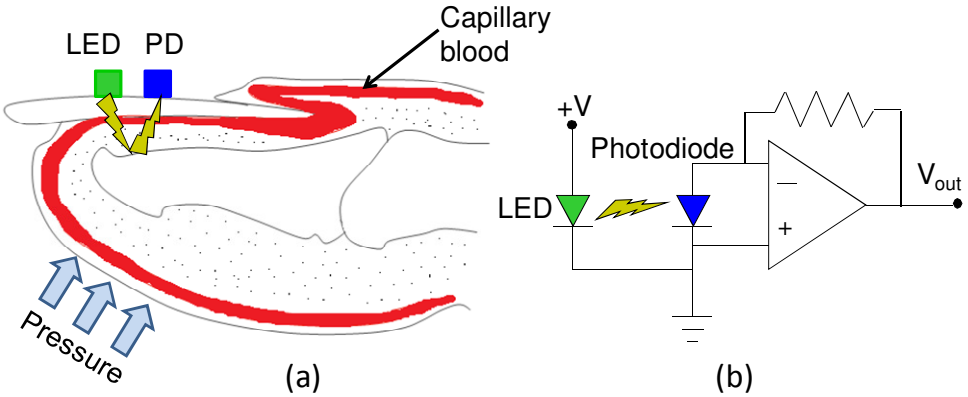

Figure 4.1 Fingernail sensor principle of operation. (a) LED and photodiode used to measure variations in fingernail coloration using (b) plethysmograph circuitry.

The original fingernail sensor had the capability of measuring normal and shear touch forces, as well as finger posture, while removing or reducing undesired effects of other extraneous variables. In the original design, miniaturized die-form optical and electrical components were mounted on a flexible Kapton printed circuit board (PCB), using wire bonding. To eliminate direct illumination between the emitters and detectors, optically opaque epoxy was placed between them. To mold the sensor to the shape of the user's fingernail, a layer of optically transparent epoxy, which covered the LEDs and photodiodes, was used. Amplifiers were placed on the top surface of the sensor, which was completely coated with optically opaque epoxy; to shield the optoelectronics from ambient light. Figure 4.2 demonstrates a fully functional fingernail sensor assembled in rigid PCB.

The miniaturized sensor was tested and analyzed by using experimental apparatus, which measures actual 3-axis fingertip touch forces and finger posture. The response of the prototype sensor was characterized for different types of forces, where the sensor responded with different patterns to each of the variables of interest [2].

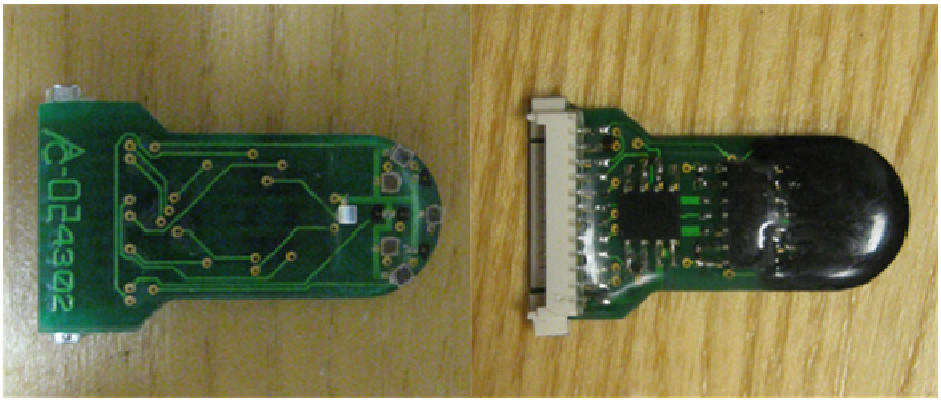

Figure 4.2 Implementation of original fingernail sensor. In the left picture, the optoelectronic devices are mounted on the bottom side of the sensor. In the right picture, the amplifiers are placed on the top side.

There are several extraneous variables that might influence the sensor's performance and accordingly should be eliminated or controlled by the physical design of the sensor. For example, using LEDs with a peak emission wavelength of 525nm removes the dependence of the light absorption coefficient of blood on oxygen saturation. Also, the light intensity of the LED can be held constant by strictly controlling the current through the LED via the use of a transistor.

However, the influence of other extraneous variables, such as the human cardiovascular status, body temperature, and hand elevation, cannot be eliminated or reduced by the physical design of the sensor. Nevertheless, the nature of the application can be selected with this in mind. For example, the fingernail sensor can be used as a wearable replacement for a computer mouse [2], where the measured normal force is used for clicking and shear forces control the position or velocity of a pointer on a computer screen. This application does not require strenuous or energetic activity, is usually used in mild and constant ambient temperatures, and involves minimal changes in hand elevation.

Similarly, the fabrication process of the novel stretchable fingernail sensor will provide it with the capability of fingertip force detection, while eliminating or minimizing undesired effects of the extraneous variables. Most importantly, the stretchable sensor will overcome the dependence of the original sensor on fingernail geometry, while maintaining desirable electromechanical properties.

In this paper, novel fabrication techniques are proposed as a solution to the several intellectual challenges encountered in the process of stretchable sensor fabrication. Mainly, we overcome the challenges of patterning conductive lines on a

stretchable substrate, and embedding rigid optical components in a stretchable platform, while maintaining electrical conductivity. A finite element analysis is conducted to optimize the reliability of the electrical connections by characterizing the electrical contact resistance as a function of bending curvature and substrate thickness. Finally, a prototype stretchable sensor, with an embedded LED/photodetector pair, is built and tested in relation to the design parameters.

Fabrication of Stretchable Fingernail Sensor

It is desired to fabricate a stretchable fingernail sensor which is independent of the finger geometry. Conventional flexible printed circuits can only bend in one dimension at a time, making them unsuitable for the two-dimensional curvature of the human fingernail. Hence, a stretchable fingernail sensor, which fully conforms to the fingernail surface, is developed.

Patterning Conductive Lines on a Stretchable Platform

Stretchable electronics is an emerging field, where several fabrication techniques have been recently developed to allow patterning conductive lines on an elastomeric rubber substrate, while maintaining integrity when stretched [3-6]. PDMS (polydimethylsiloxane) rubber substrate is a favorable choice for a stretchable platform based on its durability, adjustable stiffness, biocompatibility and commercial availability [3].

Initially, we built on the method described in [4], which works by depositing conductive metal lines on a prestretched rubber substrate. The metal lines buckle and form waves, as the substrate is relaxed. The substrate can be repeatedly stretched and

relaxed without compromising the circuit. We expanded on this method by prestretching the substrate radially to provide the patterned circuit with 2-D stretchability. Namely, we evaporated silver through an electrostatic mask of the desired circuit pattern to deposit thin-film conductive lines (70nm) on a PDMS substrate [7, 8]. This technique demonstrated potential utility for stretchable circuit fabrication as the conductive lines had a resistance of less than 100Ω for areal strain ($\Delta A/A$) cycled between 0 and 20% [9]. However, the fabrication process was intricate and the deposited conductive lines were exceedingly delicate making them unreliable at times.

Although PDMS is a nonconductive elastomer, it can be made conductive through the addition of conductive fillers such as carbon nanotubes, carbon black or metallic powders [10-13]. Here, we propose using a novel nanostructured nickel filler – nickel nanostrands – for fabrication of PDMS-based stretchable circuits. The Ni nanostrands have been shown to yield high sheet conductivities at low filler volume fractions in elastomeric composites [10]. The Ni nanostrand material is produced using a proprietary chemical vapor deposition (CVD) process that results in a tree-like nanostructure with a volume fraction of less than 0.5% nickel, as shown in Figure 4.3.

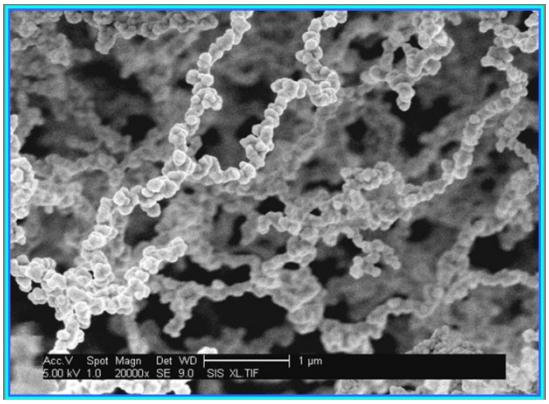

Figure 4.3 SEM micrograph of a typical interconnected Ni nanostrand structure (from Nathan Hansen, with permission).

This branching structure results in composites with unique electrical properties [10]. Of particular significance for our stretchable circuit application is that the electrical conductivity for a given loading of Ni nanostrands is higher than expected from volume percent predictions. In order to optimize the electrical conductivity, 15 vol% filler fractions have been mixed into uncured SR Stretch elastomer, which is then cast into a thin sheet via doctor blading. After curing, a stretchable substrate is added to the conductive sheet by casting liquid PDMS on the top side, followed by a curing step. The desired circuit is patterned on the bottom side of the conductive sheet using a laser cutter – a novel approach that eliminates photolithography steps.

Since the conductive sheet and stretchable substrate are composed of different elastomers, the bond between the two layers is weak. Hence, when the laser cuts the circuit pattern in the conductive layer, the extra conductive rubber can be simply peeled off the PDMS substrate, leaving the desired stretchable conductors incorporated into the stretchable substrate. Figure 4.4 illustrates the proposed process for fabricating the stretchable conductive lines used for power transmission and signal acquisition from the sensor's embedded optoelectronic components.

Embedding Rigid Optoelectronic Devices in a Stretchable Platform

In order for the entire sensor to be stretchy, bonded connections between the stretchable conductors and the rigid optical components (LEDs and photodiodes) must be avoided. Accordingly, we propose creating cavities for the optoelectronic devices in a second layer of PDMS on top of the prepatterned stretchable conductors, such that the embedded devices make electrical contact with the underlying conductors without being bonded, and the entire circuit can be stretched for many cycles [7, 8, and 9].

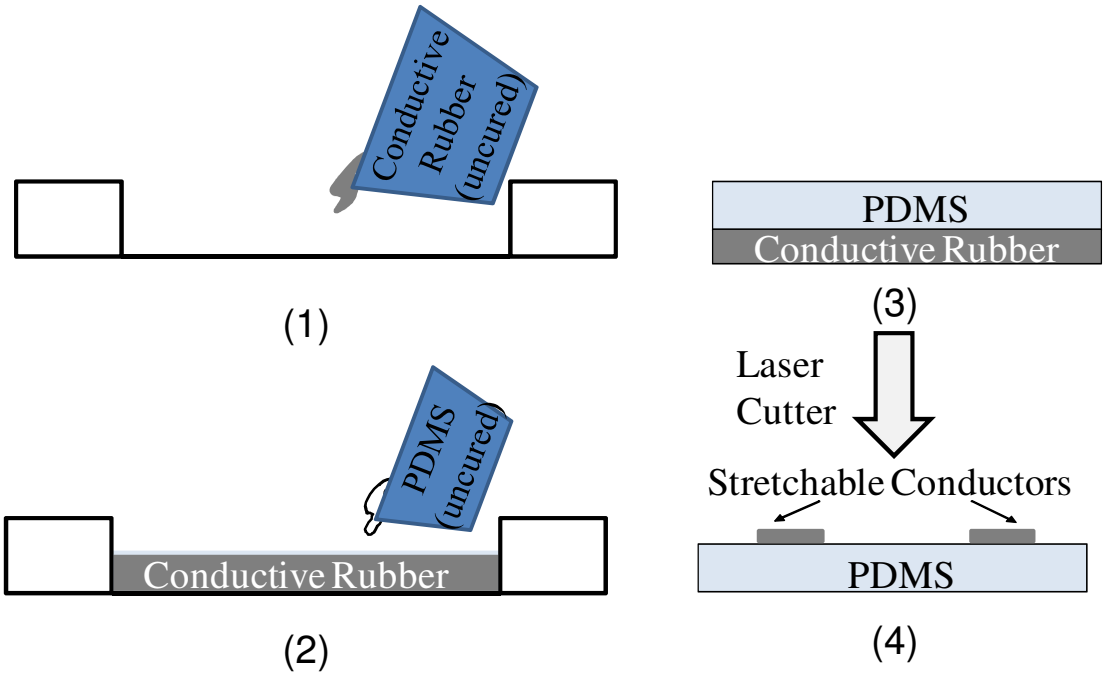

Figure 4.4 Fabrication process for patterning conductive lines on a stretchable substrate.

Figure 4.5 illustrates the fabrication steps of this novel concept. We first bond a surface mount device (SMD) upside down onto a rigid plate, and then place it on top of the stretchable circuit. During the embedding process, the optoelectronic components are preloaded to maintain electrical contact between the components and the underlying patterned lines. We pour uncured PDMS around the SMD to create the desired cavity. Once the PDMS layer cures, the SMD is removed and the deformed PDMS relaxes, shrinking the cavity. The formed cavity will expand to accommodate a subsequently inserted functional SMD and the reliability of the electrical connections is expected to be assisted by the concave bending of the substrate, when loaded onto the fingernail surface [7, 8, and 9].

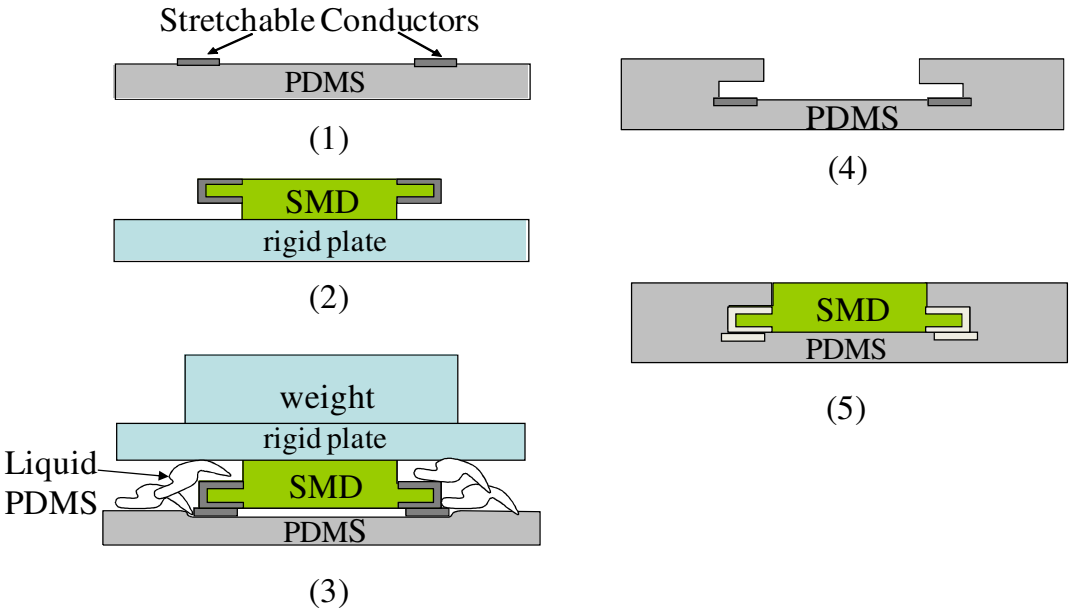

Figure 4.5 Steps of embedding a surface mount device in a second PDMS layer on top of the patterned stretchable circuit.

Stretchable Fingernail Sensor Prototype

Figure 4.6 demonstrates a photodiode and LED embedded in a second layer of pigmented PDMS on top of the prepatterned conductive lines. The concave bending of the stretchable sensor prototype, when loaded onto the convex fingernail surface, assists the electrical connection as indicated by the illuminated LED.

Recently, nonhazardous liquid metal (eGaIn) has been incorporated into the

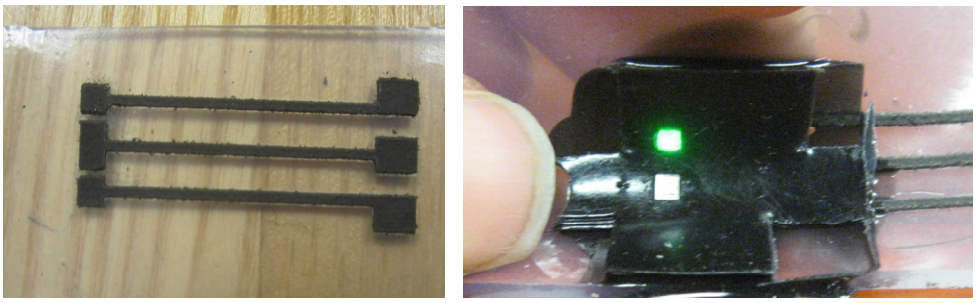

Figure 4.6 Stretchable circuit and embedded LED/photodiode pair. The concave bending of the stretchable sensor prototype assists the electrical connection. PDMS is pigmented to shield the sensor from ambient light.

fabrication of stretchable circuits as an electrical interconnect for purposes of power transmission and signal acquisition due to its low electric resistivity [14-18]. In a method similar to that used to embed the optoelectronic devices, we can create wells to be filled with liquid metal, where a rigid wire is inserted into the cavity and secured by adding a final PDMS layer [7, 8, and 9].

However, our stretchable circuit is designed such that the electrical interface is not subject to bending, and therefore is not required to be stretchable. The durable conductive lines are simply attached to toothless alligator clips for power transmission and signal acquisition.

Finite Element Analysis

To optimize the fabrication parameters of the stretchable fingernail sensor, we conduct a finite element analysis. In particular, it is desired to investigate the electrical conductivity between the optoelectronic devices and the underlying stretchable conductors in relation to the bending curvature and substrate thickness.

In order to model the behavior of the electrical contact as the sensor is mounted onto the convex fingernail surface, it is desired to identify the range of the radius of fingernail curvature in the transverse direction. A recent study measures transverse nail curvature for 92 men and 90 women, aged 21-90 years, to evaluate the influence of gender, age, and hand size and dominance on the transverse fingernail curvature [19]. Figure 4.7 shows the average Radii of transverse fingernail curvature with error bars corresponding to the standard deviations.

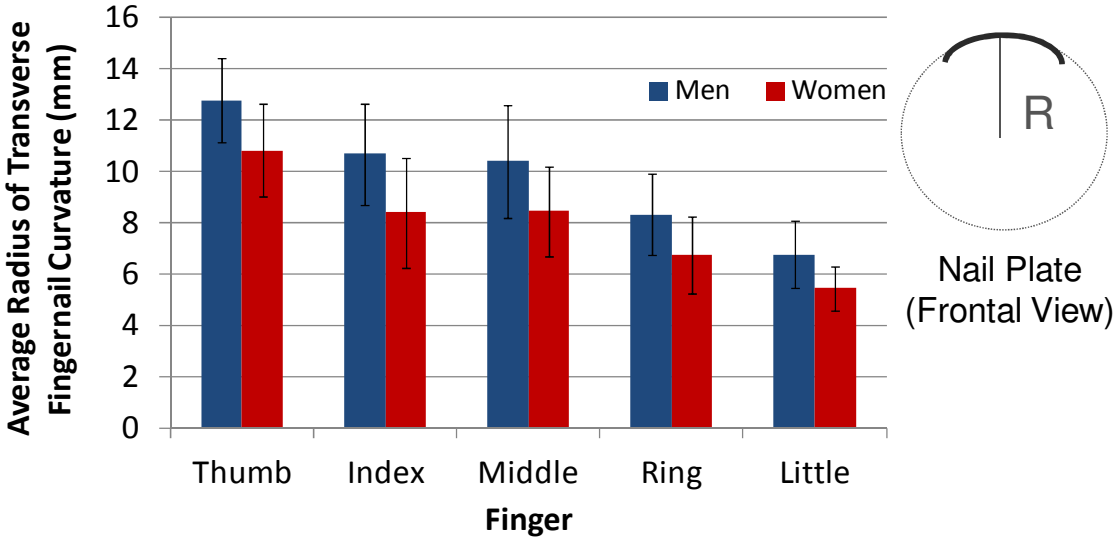

Figure 4.7 Average radii of transverse fingernail curvature for 92 men and 90 women with error bars corresponding to the standard deviation. Data taken from S. Murdan [19].

The total thickness of the fabricated stretchable sensor is 2.6 mm, where the thickness of the PDMS substrate, the stretchable conductors, and second PDMS layer are 1.1mm, 0.4mm, and 1.1mm, respectively. For simplicity, we model one embedded surface mount device with the dimensions of our choice of photodiode, a Young's modulus of 3.1MPa, and a Poisson's ration of 0.33. The PDMS and stretchable conductors are modeled as one linear elastic material of a Young's modulus of 360KPa, and a Poisson's ratio 0.4999.

Since the stretchable sensor is mainly bent along one axis, a 2-dimensional plane stress model is used along with axis symmetry. Figure 4.8 demonstrates the finite element analysis, using COMSOL4.2, of pressure distribution in the stretchable sensor when loaded onto a fingernail curvature of a radius of 12mm.

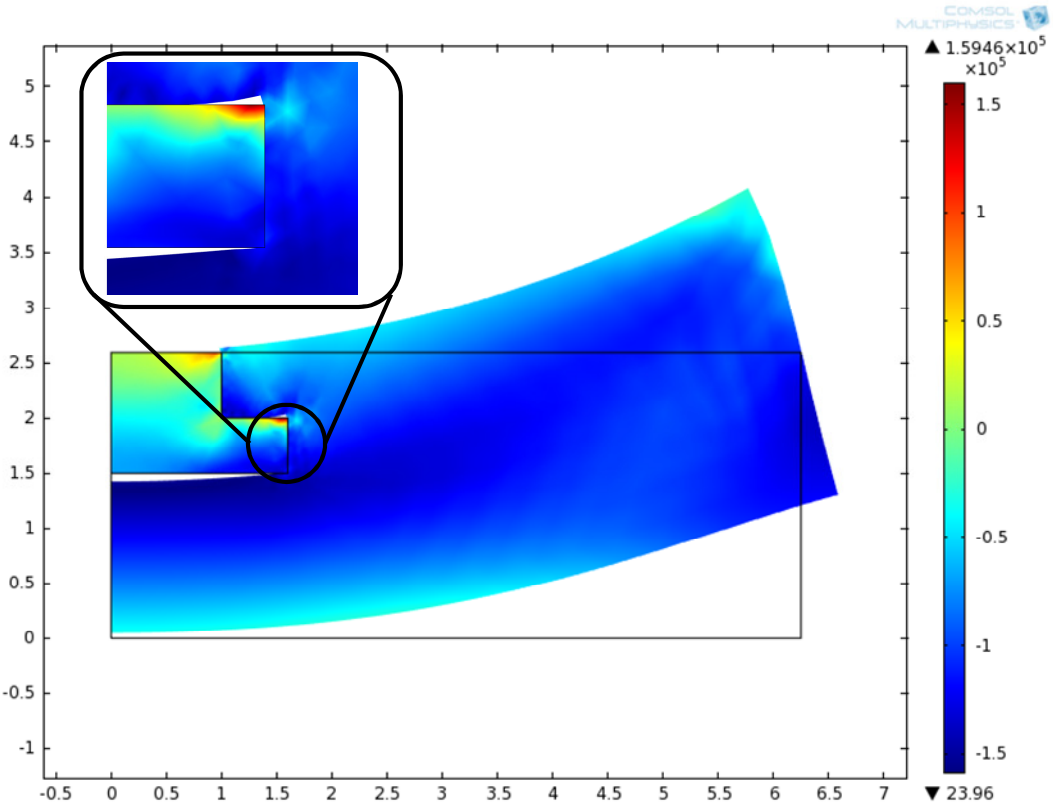

Figure 4.8 Finite element analysis of pressure distribution in the stretchable sensor when loaded onto a fingernail curvature of a radius of 12mm.

We are particularly interested in the pressure distribution along the bottom surface of the optoelectronic component, shown in Figure 4.9, given that it comes into contact with the underlying stretchable conductors. As expected, pressure increases at the edge of the optoelectronic device where it appears to come in full contact with the underlying stretchable conductors in Figure 4.8.

However, all surfaces are rough on the microscale and accordingly the actual area of contact A_c between two surfaces is independent of the area of apparent contact of the surfaces and can be evaluated by [20]

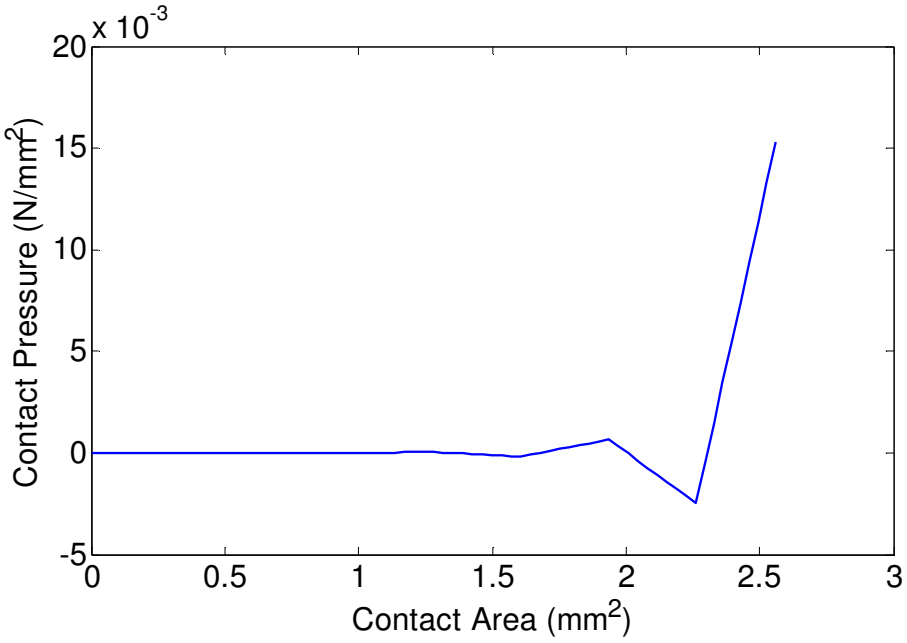

Figure 4.9 Contact pressure along the bottom surface of embedded optoelectronic device.

$$A_C = F/H \tag{4.1}$$

where F is the force acting on the electrical interface and H is the hardness of the softer material in contact (i.e., stretchable conductors) which can be approximated as 3x tensile strength [20] and is estimated to be 7.25MPa.

Equation (4.1) suggests that the actual contact area is a small fraction of the nominal contact area and is independent of the dimensions of the bodies in contact. With increased applied load the actual area of contact increases, resulting in improved electrical conductivity. As illustrated in Figure 4.10, we propose fully embedding the optoelectronic device in PDMS by adding a transparent layer of PDMS which is anticipated to increase the contact pressure between the stretchable conductors and the optoelectronic device on top of them.

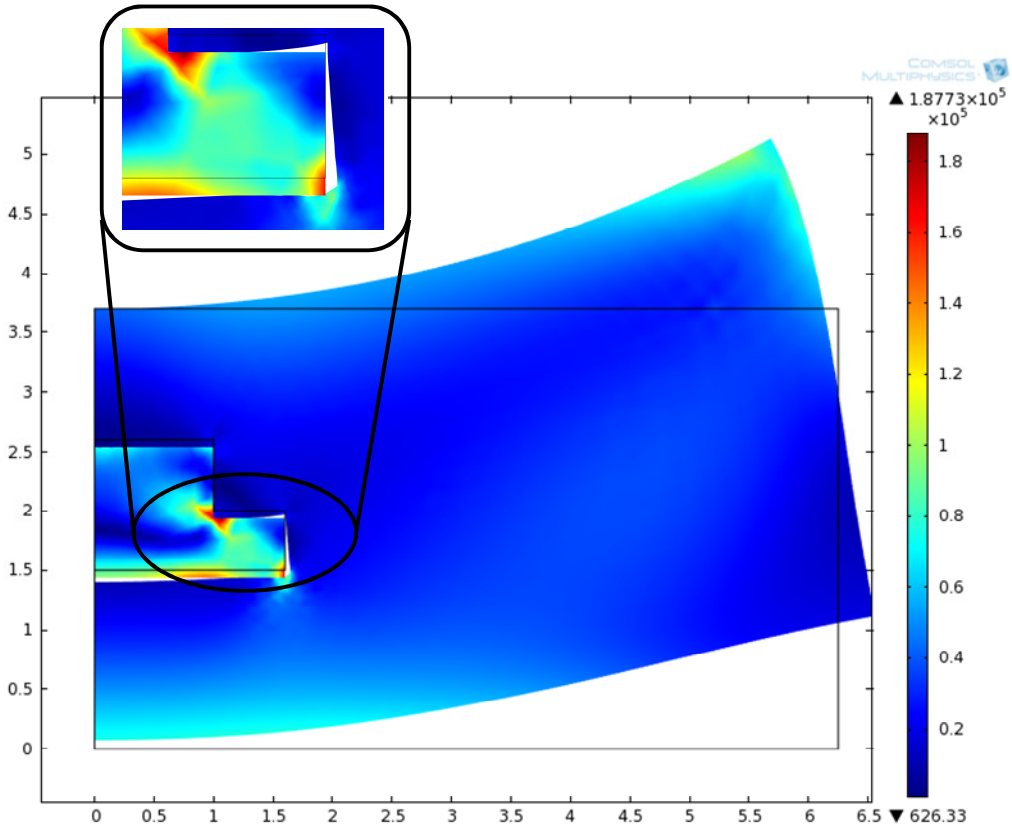

Figure 4.10 Finite element analysis of pressure distribution in the stretchable sensor with an added thickness of 1.1mm, when loaded onto a fingernail curvature of a radius of 12mm.

Visually, one can see that the nominal contact area increases as the optoelectronic device is fully embedded in PDMS compared to the stretchable sensor design in Figure 4.8. Figure 4.11 confirms that the added thickness does increase the amount of pressure distributed along the bottom surface of the optoelectronic component.

Specifically, the maximum contact pressure increases by about 5x, as a thickness of 1.1mm is added. To evaluate the actual contact area between the embedded optoelectronic device and the underlying stretchable conductors, the average applied load F is computed by finding the area under the pressure vs. contact area curve (Figures 4.9 and 4.11), as follows

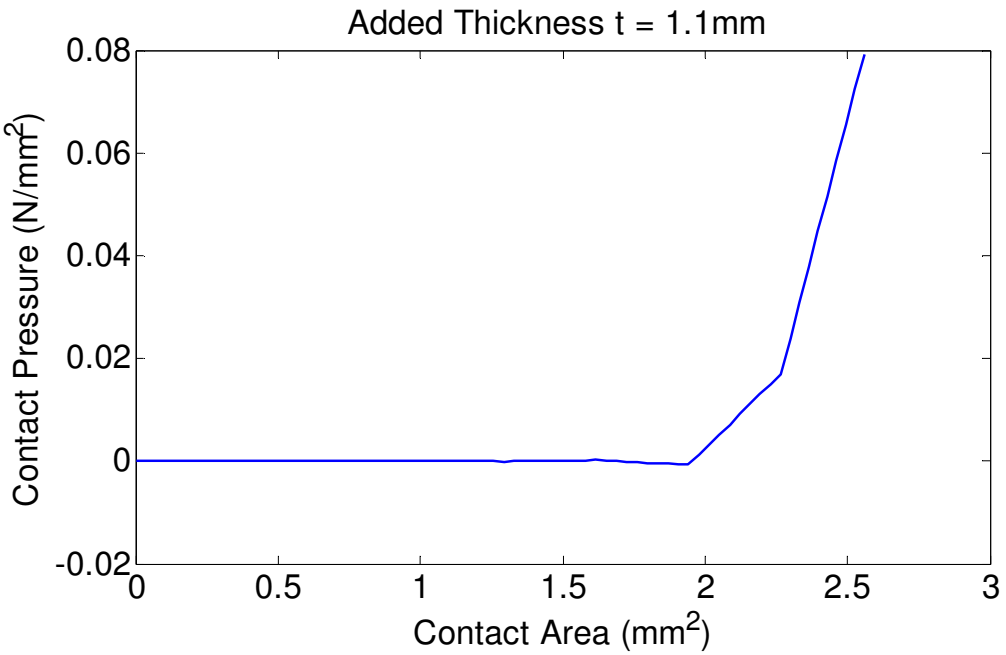

Figure 4.11 Contact pressure along the bottom surface of fully embedded optoelectronic device. The added thickness is 1.1mm.

$$F = \int_a^b \sigma \, dA \tag{4.2}$$

where a and b are the boundaries of the area of the optoelectronic device which is covered with gold conductors.

The applied force F is determined form equation (4.2) in relation to the radius of bending curvature and added PDMS thickness, as shown in Figure 4.12. Subsequently, it is used to evaluate the actual contact area A_c from equation (4.1) as demonstrated in Figure 4.13. Clearly, a larger added thickness and a smaller radius yield larger load and larger actual contact area.

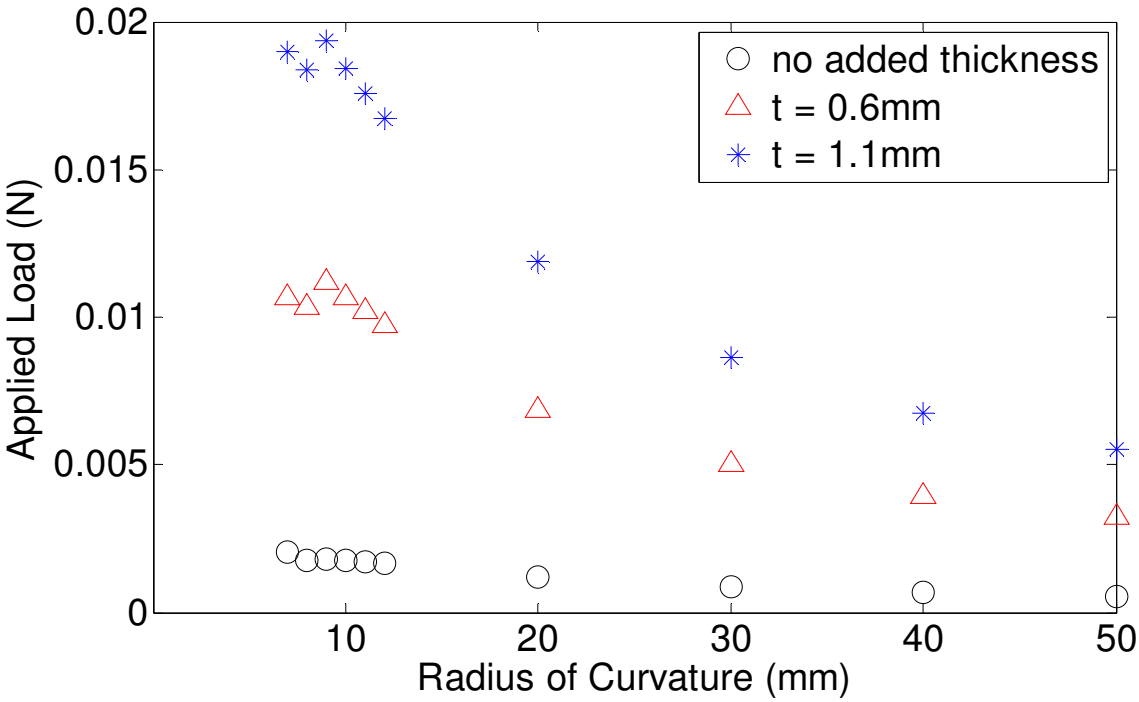

Figure 4.12 Average applied load (N) as a function of the radius of bending curvature and the added PDMS thickness.

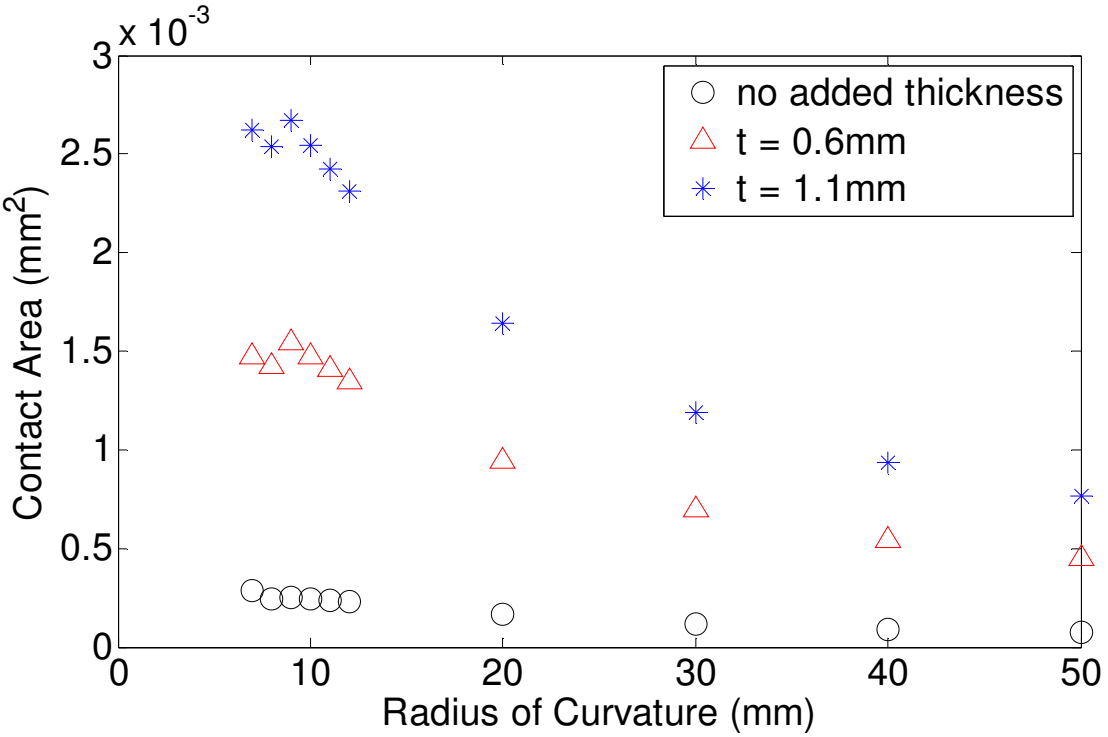

Figure 4.13 Actual contact area (mm^2) as a function of the radius of bending curvature and the added PDMS thickness.

Discussion

The average load F and the actual contact area A_c are influenced by two parameters: the radius of bending curvature and the added PDMS thickness. Evidently, fully embedding the optoelectronic device in PDMS increases the load F and accordingly from equation (4.1) enhances the actual contact area A_c, which is anticipated to improve the electrical conductivity between the surfaces in contact.

While the added PDMS thickness is controlled by the design of the stretchable sensor, the radius of bending curvature is dependent on the geometry of the fingernail. Hence, both F and A_c have been determined in relation to the added PDMS thickness under varying radius of bending curvature, as previously illustrated in Figures 4.12 and 4.13. Results indicate that a larger added thickness and a smaller radius yield larger load and larger actual contact area.

The plot in Figure 4.7 estimates the range of the radius of bending curvature that the stretchable sensor would undergo, when loaded onto the human fingernail. For this range of curvature, the variations in F and A_c in Figures 4.12 and 4.13 are minimal for each of the examined thickness conditions. The average load and actual contact area were also evaluated at larger radii to characterize the behavior of the electrical contact as a function of the bending curvature.

Electrical Contact Resistance

Fully embedding the optoelectronic device in PDMS is anticipated to improve the electrical conductivity between the surfaces in contact as the force applied to the interface as well as the contact area increase. To establish this notion, we evaluate the electrical

contact resistance in relation to the radius of bending curvature and added PDMS thickness from the following equation [21]

$$R_c = \frac{\rho_1 + \rho_2}{4\alpha} \tag{4.3}$$

where ρ_1 is the resistivity of the gold conductors on the optoelectronic device and is approximately 21.9 nΩ·m, ρ_2 is the measured resistivity of the stretchable conductors of 0.1 mΩ·m, and α is the Holm radius which can be evaluated from the actual contact area as follows [20]

$$A_c = F/H = \eta\pi\alpha^2 \tag{4.4}$$

Assuming clean interfaces, η = 1 and the contact resistance is expressed as

$$R_c = ((\rho_1 + \rho_2)/2)\{\pi H/4F\}^{1/2} \tag{4.5}$$

The decrease in contact resistance with increasing applied load is mainly attributed to the increase in the number of contacting spots between the surfaces brought to contact by increasing load [20]. The contact resistance is plotted in Figure 4.14 as a function of radius of bending curvature and added thickness. There is a noticeable reduction in the electrical resistance at smaller radius and larger added thickness. However, to avoid fabricating a relatively bulky stretchable sensor, the added thickness is capped at 1.1mm.

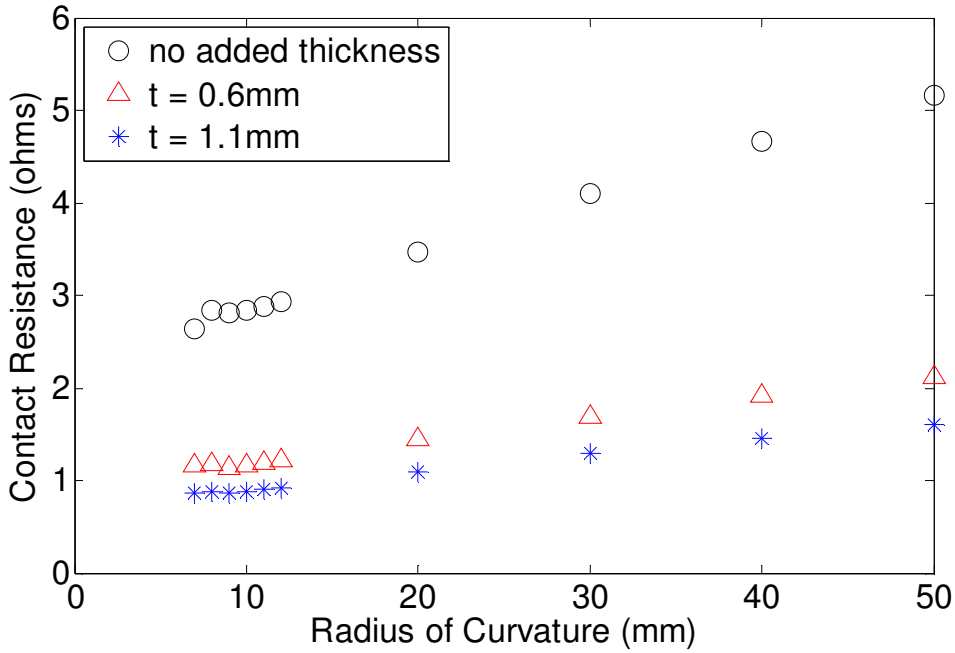

Figure 4.14 Contact resistance (Ω) as a function of the radius of bending curvature and the added PDMS thickness.

To experimentally validate that the added thickness improves electrical conductivity, we fabricate a stretchable sensor with an added thickness of 0.6mm and compare its functionality to a stretchable sensor with no added thickness. For each sensor design, we decrease the radius of bending curvature until the LED lights up. In the case of the added thickness, the LED illuminates at a radius of 15.93mm, while for no added thickness that LED does not illuminate until we arrive at a radius of 12.42mm.

This is consistent with the results in Figure 4.14 where at the same radius, the stretchable sensor with a thickness of 0.6mm has lower contact resistance when compared to a sensor with no added thickness. Accordingly, the fabrication of the stretchable fingernail sensor can be optimized based on the findings from the finite element analysis introduced in this paper.

Conclusion

Using novel fabrication techniques, we have successfully fabricated a stretchable fingernail sensor prototype which is capable of fully conforming to the two-dimensional curvature of the human fingernail, while maintaining electrical conductivity. In particular, conductive Ni nanostrand-rubber composite was patterned on a stretchable PDMS substrate, and a rigid LED/photodiode pair was embedded in a second PDMS layer on top of the prepatterned conductors.

The fabrication of the stretchable fingernail sensor is optimized based on finite element modeling, where the electrical conductivity between the optoelectronic devices and the underlying stretchable conductors is investigated. The analysis indicated that increased applied load increases actual area of contact, which is anticipated to result in improved electrical conductivity. Accordingly, we propose fully embedding the optoelectronic devices in PDMS by covering them with an added transparent layer of PDMS.

The functionality of the proposed sensor design was examined in relation to the radius of bending curvature and the added PDMS thickness. Results indicate that a larger added thickness and a smaller radius yield larger load, larger actual contact area, and smaller electrical contact resistance. The improved electrical conductivity with added thickness was also validated experimentally.

Future work will involve further refinement of the fabrication process to allow embedding as many as 4 LEDs and 5 photodiodes in the stretchable PDMS substrate to estimate fingertip force direction. The electrical conductivity of the stretchable lines will be examined in relation to line thickness and line width to enhance the circuit's

performance. While the original rigid fingernail sensor was attached to the user's fingernail using double-sided transparent adhesive tabs, this technique has some limitations when used with the proposed stretchable sensor as it is made of rubber.

Recently, biologically inspired micro- and nanoscale elastomer fiber arrays have shown great potential in repeatable adhesion applications in the area of robotics and biomedical devices [22-25]. Using a few lithography steps, fibrillar dry adhesives can be patterned on an elastomer to be attached to a smooth surface such as the fingernail surface. This technique demonstrates macroscale adhesion pressures which can be employed in the proposed stretchable fingernail sensor with further analysis.

References

[1] S. Mascaro and H. Asada, "Photoplethysmograph fingernail sensors for measuring finger forces without haptic obstruction," *IEEE Trans. on Robotics and Automation*, vol. 17, no. 5, pp. 698–708, 2001.

[2] S. Mascaro and H. Asada, "Measurement of finger posture and three-axis fingertip touch force using fingernail sensors," *IEEE Trans. on Robotics and Automation*, vol. 20, no. 1, pp. 26-35, 2004.

[3] D. Gray, J. Tien, and C. Chen, "High-conductivity elastomeric electronics," *Advanced Materials*, vol. 16, no. 5, pp. 393-397, 2004.

[4] S. Lacour, J. Jones, Z. Suo, and S. Wagner, "Design and performance of thin metal film interconnects for skin-like electronic circuits," *IEEE Electron Device Letters*, vol. 25, no. 4, pp. 179-181, 2004.

[5] J. Xiao, A. Carlson, Z.J. Liu, Y. Huag, H. Jiang, and A. Rogers, "Stretchable and compressible thin films of stiff materials on compliant wavy substrates," *Applied Physics Letters*, 93, pp. 013109 (1-3), 2008.

[6] K. Cho, J. Koh, S. Kim, W. Chu, Y. Hong, and S. Ahn, "Review of manufacturing processes for soft biomimetic robots," *International Journal of Precision Engineering and Manufacturing*, vol. 10, no. 3, pp. 171-181, 2009.

[7] J. Abu-Khalaf, J. Park, D. Mascaro, S. and Mascaro, "Stretchable fingernail sensors for measurement of fingertip force," *Proceedings of the World Haptics Conference*, pp. 625-626, 2009.

[8] S. Mascaro, D. Mascaro, J. Abu-Khalaf, and J. Park, "Method for fabricating a stretchable electronic circuit with embedded optoelectronic devices," US Patent No. 12/728,814, Filed March 2010.

[9] J. Park, S. Mascaro, and D. Mascaro, "2-D stretchable electronics with compliantly embedded rigid components," *Presented at the Materials Research Society Spring Meeting,* April 13-17, 2009, San Francisco, CA, session no. PP14.2.

[10] O. Johnson, C. Gardner, D. Fullwood, B. Adams, N. Hansen, and G. Hansen, "The colossal piezoresistive effect in nickel nanostrand polymer composites and a quantum tunneling model," *CMC: Computers, Materials, & Continua*, vol. 15, no. 2, pp. 87-112, 2010.

[11] O. Johnson, C. Gardner, D. Fullwood, B. Adams, and G. Hansen, "Deciphering the structure of nano-nickel composites," *Proceedings of SAMPE'09 Spring Symposium Conference,* vol. 54, May, 2009.

[12] G. Hansen, N. Hansen, D. and Adams, "Electrical and mechanical properties of space durable polyisocyanate resin / M55 carbon fiber / nickel nanostrand composite," *SAMPE Fall Technical Conference and Exhibition*, 2007.

[13] J. Engel, N. Chen, K. Ryu, S. Pandya, C. Tucker, Y. Yang, and C. Liu, "Multi-layer embedment of conductive and non-conductive PDMS for all-elastomer MEMS," *12th Solid State Sensors, Actuator, and Microsystems Workshop,* Hilton Head Island, SC, 4 pages, 2006.

[14] M. Dickey, R. Chiechi, R. Larsen, E. Weiss, D. Weitz, and G. Whitesides, "Eutectic Gallium-Indium (EGaIn): A liquid metal alloy for the formation of stable structures in microchannels at room temperature," *Advanced Functional Materials*, 18, pp. 1097-1104, 2008.

[15] H. Hu, K. Shaikh, and C. Liu, "Super flexible sensor skin using liquid metal as interconnect," *Proceedings of the IEEE Sensors Conference*, pp. 815-817, October 28-31, 2007.

[16] H. Hu and C. Liu, "Characterization and optimization of electrical contact between nanocomposite elastomer and metal," *Proceedings of the IEEE Solid-State Sensors, Actuators and Microsystems Conference*, pp. 1103-1105, June 21-25, 2009.

[17] H. Kim, C. Son, and B. Ziaie, "A multiaxial stretchable interconnect using liquid-alloy-filled elastomeric microchannels," *Applied Physics Letters*, 92, pp. 011904 (1-3), 2008.

[18] H. Kim, M. Zhang, and B. Ziaie, "A biaxially stretchable interconnect with liquid alloy joints on flexible substrate," *Proceedings of the 14th International Conference on Solid-State Sensors, Actuators and Microsystems*, pp. 1597-1600, June 10-14, 2007.

[19] S. Murdan, "Transverse fingernail curvature in adults: A quantitative evaluation and the influence of gender, age, and hand size and dominance," *International Journal of Cosmetic Science*, vol. 33, pp. 509–513, 2011.

[20] P.G. Slade, Electrical Contacts: Principles and Applications. New York: Marcel Dekker Inc., 1999.

[21] R.G. Holm, Electrical Contacts. Stockholm: Almqvist & Wiksells, 1946.

[22] S. Kim, M. Stiti, J.H. Hangand, and E.L. Thomas "Fabrication of bio-inspired elastomer nanofiber arrays with spatulate tips using notching effect," *8th IEEE Conference on Nanotechnology*, pp. 780-782, 2008.

[23] S. Kim and M. Sitti, "Biologically inspired polymer microfibers with spatulate tips as repeatable fibrillar adhesives," *Applied Physics Letters*, vol. 89, no. 26, pp. 261911-13, 27 Dec. 2006.

[24] M.P. Murphy and M. Sitti, "Waalbot: Agile climbing with synthetic fibrillar dry adhesives," *IEEE Int. Conf. Robotics and Automation*, pp. 1599-1600, 2009.

[25] P. Glass, H. Yong, C. Lee, E. Tworkoski, N. R. Washburn, and M. Sitti, "Biologically-inspired patterned and coated adhesives for medical devices," *Journal of Medical Devices*, vol. 3, no. 2, pp. 027537, June 2009.

CHAPTER 5

CONCLUSION AND FUTURE WORK

Summary of Contributions

This dissertation introduced the optimization of a novel stretchable fingernail sensor for detecting fingertip touch force direction. This research seeks to directly impact the area of human-machine interaction. We begin with a specific problem of fingertip touch force direction estimation, which will impact the study of human grasping and manipulation. We proposed the implementation of stretchable fingernail sensors to enable force direction prediction without affecting the natural human haptic sense. The outcomes of this work are also applicable to a broad spectrum of other stretchable sensors that have an analogous concept of operation, such as pulse oximeters which are used to measure pulse rate and oxygen saturation [1]. Stretchable circuits are useful for any application where a circuit must conform to a surface with arbitrary two-dimensional curvature, such as the human body. Eventually, similar sensors can also be placed on other parts of the body to monitor blood flow and perfusion.

First, the optimal optical parameters for light transmittance through the human fingernail bed have been experimentally determined in order to optimize detection of blood volume variations in the nail bed, which vary as a function of applied force. The

sensitivity and efficiency of light transmittance to wavelength and optical path length have been thoroughly investigated. Results verified that the optical parameters are optimized when using a green light (525nm) and when the surface mount LED and photodiode are placed as close together as possible (2.5mm). The light transmittance change of the fingernail bed has been also characterized for a variety of wavelength and path length combinations under varying force. Though results did not explicitly identify green as the optimal wavelength, they marked both green and blue wavelengths as top contenders. On the other hand, results suggested that a path length of 2.5mm is optimal in terms of light transmittance change.

Secondly, an optimal redesign of the optoelectronic configuration of the fingernail sensor was presented, by introducing an optical model which describes light transmittance between an LED and a photodiode in the fingernail area. The model was calibrated using experimentally-determined change in light transmittance through the fingernail bed at the optimal wavelength, where a nonlinear least-squares approach was implemented to estimate the model's parameters. The calibrated optical model was used to locate 30 optimal optoelectronic pairs based on average fingernail images of 15 human subjects. The resulting optimal optoelectronic configuration was validated by examining its ability to classify the correct force direction of test images. This was achieved by implementing a two-stage classifier; in the first stage a linear discriminant multicategory classifier was applied to all force poses. The normal and positive longitudinal shear force poses were reclassified in the second stage using a pairwise classifier. With individual training, the overall classification accuracy was 93% for 15 human subjects for 6 different force poses. A reduced configuration was derived from the optimal

optoelectronic locations in order to facilitate the fabrication of the optimized fingernail sensor without significantly compromising the classification accuracy. The proposed reduced configuration resulted in an overall recognition accuracy of 95%, which is comparable to the accuracy obtained using an external camera system.

Finally, using novel fabrication techniques we have successfully designed a stretchable fingernail sensor prototype which is capable of fully conforming to the two-dimensional curvature of the human fingernail, while maintaining electrical conductivity. In particular, conductive Ni nanostrand-rubber composite was patterned on a stretchable PDMS substrate, and a rigid LED/photodiode pair was embedded in a second PDMS layer on top of the prepatterned conductors. The fabrication of the stretchable fingernail sensor was optimized based on finite element modeling, where the electrical conductivity between the optoelectronic devices and the underlying stretchable conductors was investigated. The analysis indicated that increased applied load increases actual area of contact, which is anticipated to result in improved electrical conductivity. Accordingly, the optoelectronic devices were fully embedded in PDMS by covering them with an added transparent layer of PDMS. The functionality of the proposed sensor design was examined in relation to the radius of bending curvature and the added PDMS thickness. Results indicated that a larger added thickness and a smaller radius yield larger load, larger actual contact area, and smaller electrical contact resistance. The improved electrical conductivity with added thickness was also validated experimentally.

Future Work

There are several potential areas of future research that could expand upon the work in this dissertation:

Sensor Redesign Based on Proposed Optoelectronic Configuration

We propose designing the next generation of fingernail sensors by embedding the proposed reduced optoelectronic configuration in a stretchable platform to eliminate the need for customized fabrication for each individual user. The performance of the sensor will be investigated in terms of its capability to predict force direction with high accuracy. With individual calibration, the classification procedure introduced in this dissertation can be applied to estimate fingertip force direction from experimental photodetector readings to experimentally validate the proposed optoelectronic configuration. Ultimately, the optimization of the optoelectronic configuration, along with using the optimal wavelength, is expected to enhance the fingernail force sensor prediction capabilities.

Refinement of Stretchable Sensor Fabrication Process

The development of a new stretchable sensor presents an intellectually rich set of challenges which requires using novel fabrication techniques, to create a fully functional stretchable circuit containing embedded optoelectronic components. Future work will involve further refinement of the fabrication process to allow embedding as many as 5 LEDs and 4 photodiodes in the stretchable PDMS substrate to estimate fingertip force direction. The electrical conductivity of the stretchable lines will be examined in relation to line thickness and line width to enhance the circuit's performance.

While the original rigid fingernail sensor was attached to the user's fingernail using double-sided transparent adhesive tabs, this technique has some limitation when used with the proposed stretchable sensor as it is made of rubber. Recently, biologically inspired micro- and nanoscale elastomer fiber arrays have shown great potential in

repeatable adhesion applications in the areas of robotics and biomedical devices [2-5]. Using a few lithography steps, fibrillar dry adhesives can be patterned on an elastomer to be attached to a smooth surface such as the fingernail surface. This technique demonstrates macroscale adhesion pressures which can be employed in the proposed stretchable fingernail sensor with further analysis.

Wearable Computer Mouse

A target application for fingertip force measurements using the fingernail sensor is a wearable replacement for a computer mouse [6], where the measured shear forces control the position or velocity of a pointer on a computer screen and the measured normal force controls the action of clicking. The improved classification accuracy of the proposed intelligent optoelectronic configuration validates its use for fingertip force direction estimation. It is also comparable to the original optoelectronic configuration which could measure shear forces with a root mean square error (rms) of 0.5N [6], which is approximately 10% of the applied shear force range. This suggests that with individual calibration, implementing the proposed configuration in a stretchable circuit makes it useful for a wearable replacement for a computer mouse.

References

[1] Y. Mendelson and B.D. Ochs, "Noninvasive pulse oximetry utilizing skin reflectance photoplethysmography," *IEEE Transactions on Biomedical Engineering*, vol. 35, no. 10, pp. 798-805, 1988.

[2] S. Kim, M. Stiti, J.H. Hangand, and E.L. Thomas "Fabrication of bio-inspired elastomer nanofiber arrays with spatulate tips using notching effect," *8th IEEE Conference on Nanotechnology*, pp. 780-782, 2008.

[3] S. Kim and M. Sitti, "Biologically inspired polymer microfibers with spatulate tips as repeaTable fibrillar adhesives," *Applied Physics Letters*, vol. 89, no. 26, pp. 261911-13, 27 Dec. 2006.

[4] M.P. Murphy and M. Sitti, "Waalbot: Agile climbing with synthetic fibrillar dry adhesives," *IEEE Int. Conf. Robotics and Automation*, pp. 1599-1600, 2009.

[5] P. Glass, H. Yong, C. Lee, E. Tworkoski, N. R. Washburn, and M. Sitti, "Biologically-inspired patterned and coated adhesives for medical devices," *Journal of Medical Devices*, vol. 3, no. 2, p. 027537, June 2009.

[6] S. Mascaro and H. Asada, "Measurement of finger posture and three-axis fingertip touch force using fingernail sensors," *IEEE Trans. on Robotics and Automation*, vol. 20, no. 1, pp. 26-35, 2004.